

Article

Geology, Geochronology and Geochemistry of Weilasituo Sn-Polymetallic Deposit in Inner Mongolia, China

Fan Yang ^{1,2}, Jinggui Sun ^{1,*}, Yan Wang ², Junyu Fu ², Fuchao Na ², Zhiyong Fan ³ and Zhizhong Hu ⁴

¹ College of Earth Sciences, Jilin University, Changchun 130061, China; fanyang19870509@163.com

² Shenyang Geological Survey Center, CGS, Shenyang 110034, China; wy68413@163.com (Y.W.); fjzyxy@163.com (J.F.); fuchaona1986@sina.com (F.N.)

³ Inner Mongolia Weilasituo Mining Industry Co. Ltd., Chifeng 025350, China; brkyf98@163.com

⁴ Chengdu Geological Survey Center, CGS, Chengdu 610000, China; hzz_pot@aliyun.com

* Correspondence: sunjinggui@jlu.edu.cn; Tel.: +86-024-86002927

Received: 2 December 2018; Accepted: 10 February 2019; Published: 12 February 2019



Abstract: The recently discovered Weilasituo Sn-polymetallic deposit in the Great Xing'an Range is an ultralarge porphyry-type deposit. The mineralization is closely associated with an Early Cretaceous quartz porphyry. Analysis of quartz porphyry samples, including zircon U-Pb dating and Hf isotopes, geochemical and molybdenite Re-Os isotopic testing, reveals a zircon U-Pb age of 138.6 ± 1.1 Ma and a molybdenite Re-Os isotopic age of 135 ± 7 Ma, suggesting the concurrence of the petrogenetic and metallogenic processes. The quartz porphyry has high concentrations of SiO_2 (71.57 wt %–78.60 wt %), Al_2O_3 (12.69 wt %–16.32 wt %), and $\text{K}_2\text{O} + \text{Na}_2\text{O}$ (8.85 wt %–10.44 wt %) and A/CNK ratios from 0.94–1.21, is mainly peraluminous, high-K calc-alkaline I-type granite and is relatively rich in LILEs (large ion lithophile elements, e.g., Th, Rb, U and K) and HFSEs (high field strength elements, e.g., Hf and Zr) and relatively poor in Sr, Ba, P, Ti and Nb. The zircon $\epsilon_{\text{Hf}}(t)$ values range from 1.90 to 6.90, indicating that the magma source materials were mainly derived from the juvenile lower crust and experienced mixing with mantle materials. Given the regional structural evolution history, we conclude that the ore-forming magma originated from lower crust that had thickened and delaminated is the result of the subduction of the Paleo-Pacific Ocean. Following delamination, the lower crustal material entered the underlying mantle, where it was partially melted and reacted with mantle during ascent. The deposit formed at a time of transition from post-orogenic compression to extension following the subduction of the Paleo-Pacific Ocean.

Keywords: zircon U-Pb dating; molybdenite Re-Os dating; zircon Hf isotopes; Weilasituo Sn-polymetallic deposit; Inner Mongolia

1. Introduction

The southern Great Xing'an Range (SGXR) in southeastern Inner Mongolia is part of the eastern section of the Central Asian Orogenic Belt (Xing'anling Mongolian Orogenic belt). The SGXR is a superimposed compound structural region that has experienced processes associated with the evolution of the Paleo-Asian Ocean and the subduction of the Paleo-Pacific Ocean [1–3]. Multistage tectonic, magmatic, sedimentary and metamorphic events characterize the metallogenic background of the SGXR and have resulted in the development of extensive granitic plutonic rocks, intermediate-acidic volcanic-sedimentary rocks and Paleozoic strata [4–6]. Additionally, these events have given rise to associated porphyry-type molybdenum deposits, magmatic hydrothermal vein-type Sn-polymetallic (Pb-Zn-Ag) deposits, and skarn-type Pb-Zn-Ag deposits (Figure 1). The metallogenic

ages of these deposits are mostly concentrated in the (I) Mid-Triassic (244–234 Ma; e.g., the Laojiagou Mo deposit and Baiyinnuoer Ag-Zn deposit; [7,8]), (II) Early to Mid-Jurassic (179 Ma; e.g., the Mengentaolegai Ag-Pb-Zn deposit; [9]), (III) Late Jurassic (150–153 Ma; e.g., the Budunhua Cu deposit, Hashitu Mo deposit, Jiguanshan Mo deposit, Zhanzigou Mo deposit, Maodeng Cu-Sn deposit and Aonaodaba Ag-Cu deposit, [10–13]), and (IV) the early stage of the Early Cretaceous (141–133 Ma; the Dajing Sn-polymetallic deposit, Weilasituo Sn-polymetallic deposit, Bairendaba Pb-Zn-Ag deposit, Huanggang Sn-Fe deposit, Haobugao Fe-Zn deposit, Chamuhan Sn-polymetallic deposit, Anle Ag-Sn deposit, Aolunhua Mo deposit, Banlashan Mo deposit, Yangchang Mo deposit, Hongshanzi Mo deposit, Xiaodonggou Mo deposit, and Gangzi Mo deposit; [1,7,14–24]).

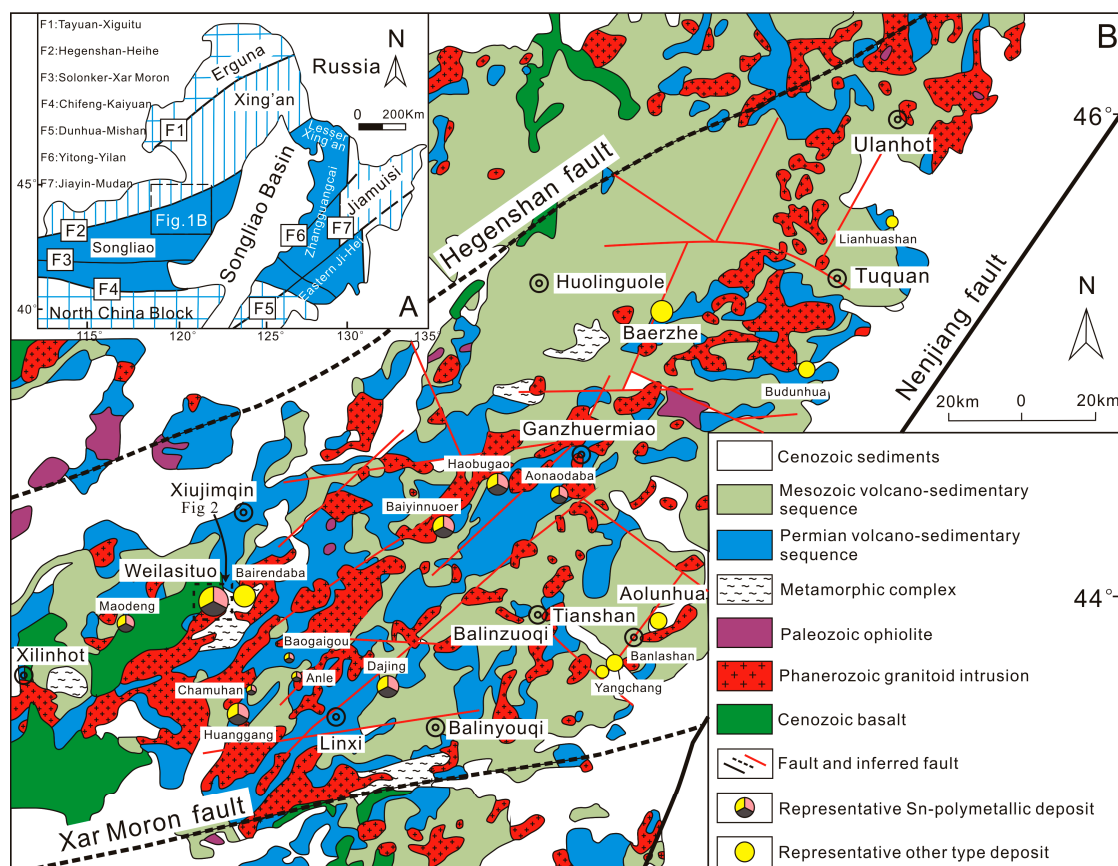


Figure 1. (A) Tectonic map of northeastern China (modified after [25]). (B) Simplified geologic map of the southern Great Xing'an Range (modified after [26]).

The Weilasituo deposit is a large recently discovered porphyry-type Sn-polymetallic deposit in the SGXR. Notably, most Sn-polymetallic deposits in this area are hydrothermal vein-type deposits and the porphyry-type Sn-polymetallic deposits are rare. The Weilasituo porphyry-type Sn-polymetallic deposit has estimated reserves of 93,127 t Sn at 1.35%, 15,800 t W at 0.44%, 32,540 t Zn at 1.63% and 9175 t Cu at 1.91% [16]. Recent studies have examined the geological characteristics, geochemistry, geochronology, and metallogenic mechanism of the Weilasituo Sn-polymetallic deposit [16,17,27,28], and have applied several geochronological methods to constrain the timing of petrogenesis and metallogenesis. The zircon U-Pb ages of the quartz porphyry are 138 ± 2 Ma and 135.7 ± 0.9 Ma [16,27]. The molybdenite Re-Os isochron ages are 135 ± 11 Ma and 125.7 ± 3.8 Ma [16,27]. The cassiterite U-Pb ages of the disseminated mineralization and vein-like mineralization are 138 ± 6 Ma and 135 ± 6 Ma, respectively [17]. Geochemical studies have determined the mineralized rock (i.e., the quartz porphyry) is a highly differentiated I-type granite by fractional crystallization [17].

In this contribution, we present LA-ICP-MS zircon U-Pb ages, molybdenite Re-Os ages, new whole-rock elemental compositions of the quartz porphyry and in situ zircon Hf isotopic data for the Weilasituo Sn-polymetallic deposit. We integrate these data with the results of previous research, enabling us to constrain the petrogenesis of the quartz porphyry and the mineralization timing of the deposit to evaluate the relationships between magmatism and metallogeny.

2. Regional Geology

The Weilasituo Sn-polymetallic deposit is located in the SGXR and is separated from the northern edge of the North China Block by the Xar Moron Fault to the south, from the Songliao Basin by the Nenjiang Fault to the east and from the Erguna-Xing'an Block by the Erlianhaote-Hegenshan Fault to the north (Figure 1B). Tectonically, this deposit forms part of the eastern side of the Central Asian Orogenic Belt (Figure 1A). From the Paleozoic through the Triassic, the area was influenced by the evolution of the Paleo-Asian Ocean [29], and experienced multiple collisions, accretion and regional extension events [30–33]. The SGXR was influenced by the subduction of the Paleo-Pacific Ocean during the Mesozoic [11,32], resulting in collision-related compression after extension, and also widespread late Mesozoic granitoids and volcanic rocks [11,33,34].

The oldest strata in the area consist of a Paleozoic, intermediate to high-grade metamorphic complex termed the “Xilin hot complex”, which comprises amphibolite, plagioclase-bearing gneiss, mica schist and biotite-bearing granitic gneiss. In addition, Ordovician, Silurian, Devonian and Carboniferous clastic sedimentary, volcanic and carbonate rocks also crop out in the area [22]. The Permian volcanic-sedimentary strata are composed of carbonaceous clastic, volcanic and carbonate rocks [35].

The Paleozoic strata are intruded by Hercynian–Yanshanian granitic plutons and are overlain by Mesozoic volcanic-sedimentary sequences [36]. Paleozoic granitoids, tonalite, diorite and granodiorite, are chiefly located in the western part of the SGXR (Figure 1A), and the ages of zircon U-Pb range 321–237 Ma [28]. These granitoids comprise a post-subduction, high-potassium calc-alkaline magmatic suite and were generated under the geodynamic regime produced by the slab break-off of the Paleo-Asian Ocean [37]. The Mesozoic granitoids include monzogranite, granodiorite, and syenogranite, with ages ranging 150–131 Ma [28]. These granitoids show positive ϵ_{Nd} values, suggesting that the pre-existing juvenile and ancient crustal components underwent remelting, recycling, and redistribution [38].

Mesozoic volcanic-sedimentary sequences are the stratigraphically highest rocks in the SGXR (Figure 1B). From bottom to top, these volcanic rocks can be subdivided into Manketouebo, Manitu, Baiyingaolao, and Meiletu Formations [39,40]. Zircon U-Pb ages show that Mesozoic volcanic activity occurred throughout the SGXR and began in the Late Jurassic and peaked in the Cretaceous [26]. Geochemically, these volcanic rocks are diverse, including trachyandesites, basaltic trachyandesites, rhyolites and trachytes, with smaller quantities of dacites and basalts [26]. The chemical properties of the mafic-intermediate rocks are similar to basalts formed in an intraplate extensional zone. The mafic-intermediate rocks have the characteristics of slightly enriched Sr isotope ratios and weakly depleted to slightly enriched Nd isotope ratios. These features show that the mafic-intermediate rocks were derived from weakly depleted to enriched continental lithospheric mantle [41].

3. Deposit Geology

In addition to the extensively exposed Holocene strata, the other rocks in the area include the Xilin hot complex, quartz diorite, cryptoexplosive breccia and buried quartz porphyry (Figure 2A,B). The Xilin hot complex is a combination of brown amphibole–plagioclase and biotite–plagioclase gneiss, both intensely metamorphosed and deformed. The quartz diorite is less extensively exposed and subject to NE-trending faults [42]. The cryptoexplosive breccia is spatially linked with the quartz porphyry in the upper part and it usually occurs at the contact between the Xilin hot complex and the quartz porphyry [17]. The buried quartz porphyry, whose overall morphology is unknown to date, lies

approximately 400 m beneath the surface. The quartz porphyry samples recovered from a drillhole have an off-white color, a massive structure and a porphyritic texture (Figure 3A,B). The main minerals are K-feldspar (65%–70%), quartz (25%–27%) and biotite (3%–5%).

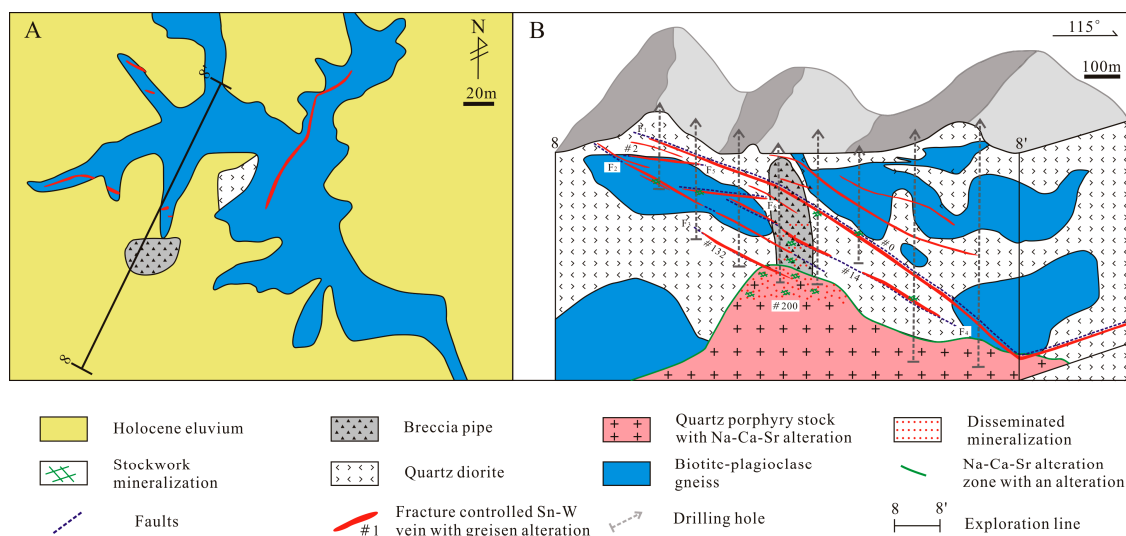


Figure 2. (A) Geological sketch map of the Weilasituo Sn-polymetallic deposit; (B) Schematic map of main orebodies of the Weilasituo Sn-polymetallic deposit (modified after [17]).

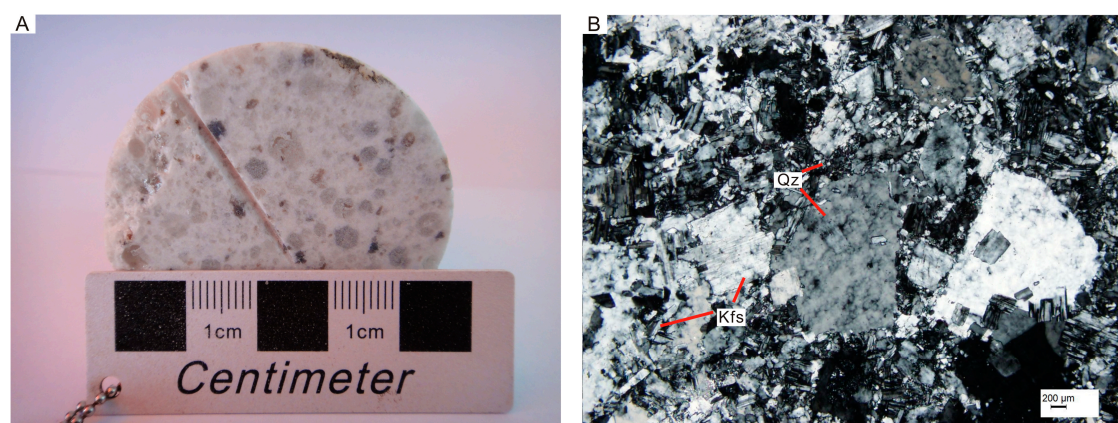


Figure 3. (A) Characteristic features of quartz porphyry; (B) Photomicrographs of quartz porphyry. Abbreviations: Qz—quartz; Kfs—K-feldspar.

The faults in the area trend primarily NE–SW and secondarily sub-E–W (Figure 2B). They are developed in the quartz diorite and, as the main ore-controlling structures, provided spaces for mineralization. The NE-trending faults F_1 , F_2 , F_3 and F_4 strike 20° – 43° , dip from 18° – 35° , and extend approximately 30–900 m with widths of 0.3–14 m. The E–W-trending faults (F_5 and F_6), located above or outside of the quartz porphyry, strike 85° – 115° , dip 20° – 25° , and extend approximately 20–800 m [17].

Mineralization and Alteration

The mining area is currently under mineral exploration, and ores have been encountered and verified by drilling. Ore bodies in the area come in three forms: (I) shallow quartz vein-type ore bodies, (II) moderate-depth cryptoexplosive breccia-type ore bodies, and (III) deep quartz porphyry-type ore bodies (Figure 2B).

Fifteen shallow quartz vein-type ore bodies of medium size or greater have been detected. These vein-like or stratiform subparallel ore bodies strike 25° – 205° , dip towards 115° at 11° – 54° , and

exhibit a fairly simple morphology with basically continuous strike and some branching-reconnecting along dip. These orebodies extend 32–1400 m horizontally and 43–1300 m vertically, and their thicknesses range from 0.1 to 13 m. The cryptoexplosive breccia-type ore bodies are found in the cryptoexplosive breccia. Their morphology is associated with the internal structural morphology of the cryptoexplosive breccia. Local quartz vein-type ore bodies are found to cut the breccia-type ore bodies, adding to the complexity of these ore bodies. The quartz porphyry-type ore bodies found at the upper contact of the quartz porphyry bodies occur in lenticular form and are morphologically similar to the ore bodies above the quartz porphyry bodies, and those found inside the quartz porphyry bodies occur in a vein-like form. Seven ore bodies of industrial size, represented by Sn #200 (Figure 2B), represent more than 80% of the total quartz porphyry-type ore-body resources in the area. The ore bodies vary in size, extending dozens of meters to 400 m horizontally and 70 m vertically. Their thickness ranges from 1 to 10 m.

Three types of mineralization that are recognized in the Weilasituo deposit: stockwork mineralization, disseminated mineralization and vein-like mineralization. Stockwork mineralization exists both inside and outside the quartz porphyry and inside the cryptoexplosive breccia pipe. Disseminated mineralization occurs in the quartz porphyry. Vein-like mineralization occurs outside the quartz porphyry and inside the cryptoexplosive breccia pipe.

The mineralization level decreases with increasing depth. Stockwork and disseminated mineralization have resulted in disseminated and vein-like ores (Figure 4A–D). The ore minerals are mainly cassiterite + wolframite + sphalerite with lower amounts of chalcopyrite + arsenopyrite + tetrahedrite. Disseminated mineralization is the most important form of mineralization (Figure 4H–L). Vein-like mineralization is typically found in cracks and faults on top or outside of the quartz porphyry (Figure 2B) and is responsible for vein-like ores. The ore minerals include cassiterite + wolframite + sphalerite and less amounts of chalcopyrite + tetrahedrite + pyrrhotite + molybdenite + galena. Breccia pipe mineralization occurs in steep breccia pipes (Figures 2B and 4F), with no distinct boundary with the country rock. Disseminated and spots of cassiterite, chalcopyrite and dark sphalerite occur commonly as fragments in the breccia, suggesting that the breccia mineralization occurred after the disseminated mineralization. In addition, vein-like Sn-polymetallic mineralization was found to cut into the quartz porphyry-related breccia pipe mineralization (Figure 2B), suggesting that vein-like mineralization occurred after breccia mineralization.

The Sn-polymetallic metallogenic system in the Weilasituo deposit presents a high-to-low-temperature alteration zone from the quartz porphyry outward. The center of alteration is a Na-Ca-Rb alteration combination, surrounded by greisenization with high-level Na-Ca-Rb alteration. Stockwork and disseminated mineralization can be observed, typically in the quartz porphyry-type and breccia-type ore bodies. The alteration minerals are albite + amazonite + topaz + celestine + muscovite + epidote + fluorite (Figure 4A–C). Greisenization alteration mainly occurs in the vein-like orebodies on top or outside of the quartz porphyry, although some can also be found in the overlying breccia pipes. The alteration is controlled by fissures and faults [17]. The alteration minerals include muscovite + quartz + topaz + fluorite + zircon (Figure 4E).

According to field contacts, the ore mineral and gangue mineral combinations, and the interweaving pattern among veins, are chronologically divided into two stages of mineralization: early Na-Ca-Rb alteration-induced Sn-W-Rb mineralization and late greisenization-induced Sn-W-Rb mineralization. The mineral combination of the early stage is cassiterite + sphalerite + wolframite + stannite + tetrahedrite + chalcopyrite + arsenopyrite (Figure 4A–C) and that of the latter is quartz + cassiterite + muscovite + fluorite + wolframite + loellingite + sphalerite + chalcopyrite + galena + molybdenite (Figure 4H–L).

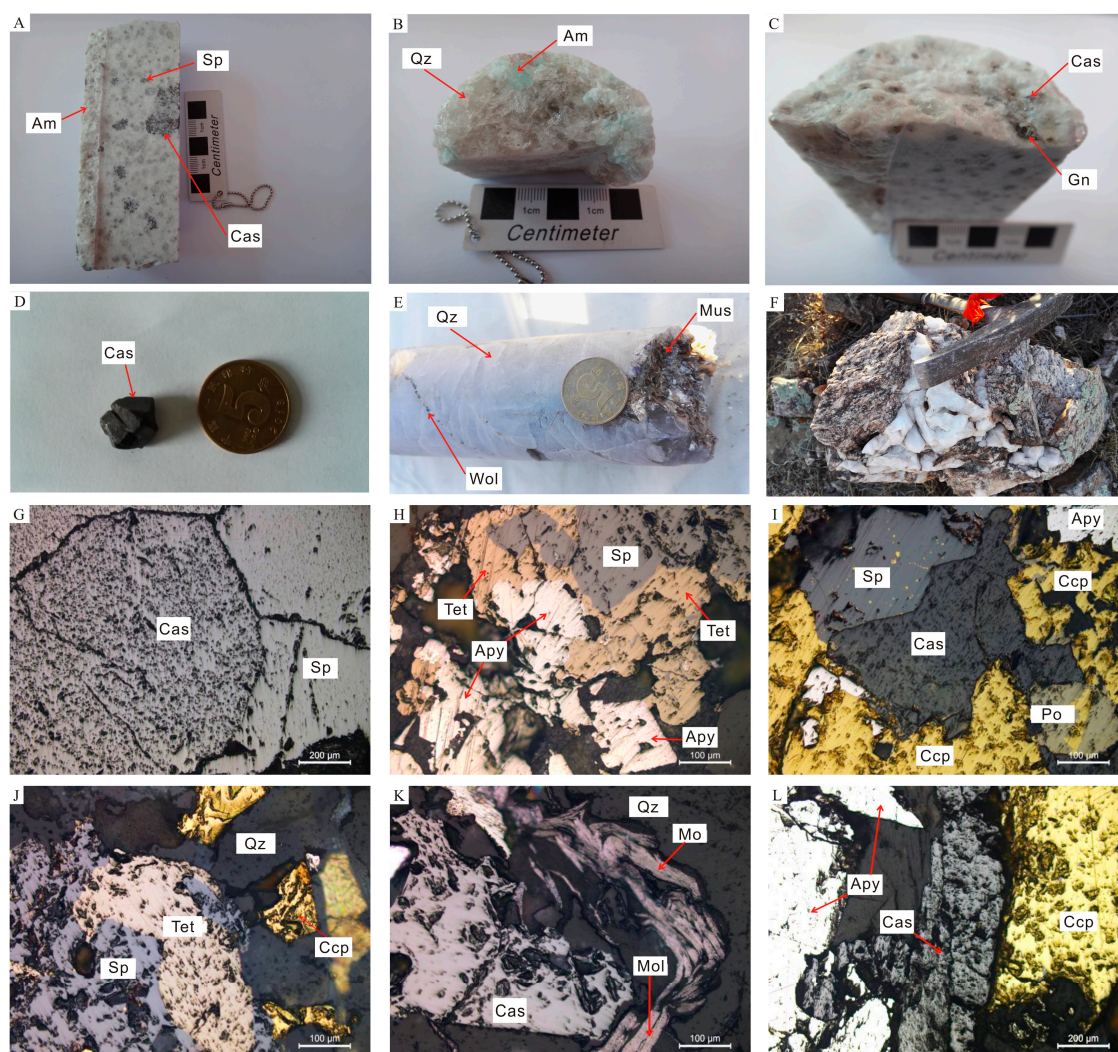


Figure 4. Photographs of mineralization features in the Weilasituo Sn-polymetallic deposit: (A) Disseminated cassiterite and sphalerite in quartz porphyry; (B) Amazonite in the quartz porphyry; (C) Cassiterite and galena in the quartz porphyry; (D) Euhedral cassiterite; (E) Typical greisen with wolframite; (F) Breccia collected from the surface; (G) Cassiterite and sphalerite intergrowths; (H) Sphalerite, arsenopyrite and tetrahedrite; (I) Cassiterite, sphaletire, arsenopyrite, pyrrhotite and chalcopyrite; (J) Greisen vein with sphaletire, tetrahedrite and chalcopyrite; (K) Greisen vein with molybdenite and cassiterite; (L) Greisen vein with cassiterite, arsenopyrite and chalcopyrite. Abbreviations: Cas—cassiterite, Am—amazonite, Apy—arsenopyrite, Ccp—chalcopyrite, Gn—galena, Po—pyrrhotite, Qz—quartz, Tet—tetrahedrite, Sp—sphalerite, Mol—molybdenite, Wol—wolframite, Mus—muscovite.

4. Sampling and Analytical Methods

Unaltered quartz porphyry samples for LA-ICP-MS U-Pb dating, zircon Lu-Hf isotope analysis and whole rock geochemistry analysis were collected from drillhole ZK809. Molybdenite samples for Re-Os isotopic analysis were also gathered from drillhole ZK809 of the porphyry Sn-W-Rb mineralization zone.

4.1. Zircon LA-ICP-MS U-Pb Dating

Two zircon U-Pb isotopic dating samples (ZK809-1 and ZK809-2) were analyzed at the Key Laboratory for Sedimentary Basin and Oil and Gas Resources, Ministry of Land and Resources. A GeoLasPro 193 nm laser system and an SF-ICPMS Element 2 were used for ablation and mass

spectrometry, respectively. High-purity He gas was used as the carrier gas for the ablated material. The test was conducted with a laser wavelength of 193 nm, a beam spot of 32 μm , a pulse frequency of 6 Hz, and a laser energy of 6 J/cm². Before the test, the instrument was tuned to the optimal state using the NIST610 standard so that the ¹³⁹La and ²³²Th signals were the highest and the oxide yield for ²³²Th¹⁶O/²³²Th was less than 0.3%. GJ-1 zircon standard specimens were used as external criteria to calibrate the fractionation and mass discrimination of U-Pb isotopes, and Plšovice zircon standard specimens were used as control specimens to monitor the stability of the analytical process. A set of standard specimens was inserted every five samples. Laser sampling of each sample included 20 s of background acquisition, 50 s of ablation sampling and 10 s of cell flushing. ICPMSDataCal was used to process the analysis data offline [43].

4.2. Molybdenite Re-Os Dating

Five molybdenite Re-Os isotope dating samples (ZK809-1 to ZK809-5) were obtained by separating the molybdenite samples collected from the drillhole (in basically the same way as for zircon) to a size far smaller than 2 mm to avoid decoupling. Re-Os isotopic testing was conducted at the Re-Os isotopic laboratory of the National Geological Test Center. A TJA X-series ICP-MS was used to determine isotopic ratios. For low Re-Os samples, a Thermo Fisher Scientific HR-ICP-MS Element 2 was used. For Re, mass numbers 187 and 185 were selected, and mass number 190 was used to monitor Os. For Os, mass numbers 186–190 and 192 were selected, and mass number 185 was used to monitor Re. Blank values of Os, Re and ¹⁸⁷Os measured by the TJA X-series ICP-MS were $(0.0031 \pm 0.0005) \times 10^{-9}$, $(0.00023 \pm 0.00008) \times 10^{-9}$, and $(0.00039 \pm 0.00005) \times 10^{-9}$, respectively, which were far smaller than the Os and Re measurements from the samples and the standard specimens and were therefore insignificant with respect to the test results. Common Os was calculated through the measured ¹⁹²Os/¹⁹⁰Os ratio according to the atomic and isotopic abundance charts. The uncertainties in Os and Re concentrations included weighing errors for the samples and thinner, calibration errors for the thinner, fractionation calibration errors for mass spectrometry, and isotopic ratio measurement errors for the samples in question. The confidence degree can reach 95%. The uncertainties in the model age also included this uncertainty (1.02%). The confidence degree was 95%. National standard materials (GBW04435 (JDC)) were used as standard specimens to monitor the reliability of the chemical process and analysis data. The principles and processes of Re-Os isotope analysis are detailed in Du et al. [44].

4.3. Whole Rock Geochemistry

Eight collected samples were crushed to 200-mesh powder. Major elements were analyzed on an Axios MaxX fluorescence spectrometer. FeO was titrated through a 50-mL burette. The sample was first placed in a Li₂B₄O₇ solution at a ratio of 1:5, melted at 1050–1250 °C, formed into thin glass sections and analyzed with approximate accuracies of 1% for SiO₂ and 2% for other oxides. Rare earth elements (REEs) and trace elements were analyzed on an X-series 2 instrument. A sample of whole-rock powder (200 mesh) weighing 50 mg was placed in a Teflon flask, dissolved with HNO₃ and HF solutions for 2 days, further dissolved by adding HClO₄, dried by distilling, and then diluted to 50 mL with a 5% HNO₃ solution before being analyzed for trace elements. During analysis, two GBW series specimens were measured: one for calibrating Li, Ba, Cr, V, Co, Ni, Zn, Cu, Ga, Sr, Rb, Cs, Ba, Pb, U, Th, Sc, Y and REEs and the other for calibrating Mo, W, Nb, Ta, Hf and Zr. The analysis errors were less than 5%. Major elements, trace elements and REEs were measured at the testing center of the Shenyang Geological Survey Center, Ministry of Land and Resources.

4.4. Zircon Lu-Hf Isotope

In situ analysis of the zircon Hf isotope composition of the quartz porphyry from the Weilasituo deposit was conducted at the State Key Laboratory for Mineral Deposits Research, Nanjing University using a Neptune Plus MC-ICP-MS equipped with a New Wave UP193 laser microprobe.

The data acquisition and instrumental conditions were similar with Wu et al. [45]. The analyses were mainly conducted with a repetition rate of 8 Hz and a beam diameter of 35 μm . Ar and He carrier gases were used to transfer the ablated sample from the laser ablation cell to the ICP-MS torch through the mixing chamber. Atomic masses 172, 173, 175–180 and 182 were measured simultaneously in the static collection mode. Corrections of isobaric interferences of ^{176}Lu and ^{176}Yb on ^{176}Hf were based on, Wu et al. [45], and Yang et al. [46]. The performance conditions and analytical accuracy were monitored by the 91500 and Mud Tank zircon standards ($^{176}\text{Hf}/^{177}\text{Hf} = 0.282507 \pm 6$ [47]). The initial Hf values (ϵ_{Hf}) were calculated by using the decay constant of 1.865×10^{-11} per year [48] for ^{176}Lu and the chondritic model with $^{176}\text{Lu}/^{177}\text{Hf} = 0.0332$ and $^{176}\text{Hf}/^{177}\text{Hf} = 0.282772$ [49]. Depleted mantle Hf model ages (T_{DM}) were calculated by using the $^{176}\text{Lu}/^{177}\text{Hf}$ ratios of the zircon. These ages refer to a model of depleted mantle with a current $^{176}\text{Lu}/^{177}\text{Hf}$ ratio of 0.28325 which is similar to the average of MORB [50], which has a $^{176}\text{Lu}/^{177}\text{Hf}$ ratio of 0.0384 [51] and assumes an average continental crust ratio (f_{CC}) of -0.55 [52].

5. Results

5.1. Zircon U-Pb Dating

Pb isotopic age analysis was conducted on 52 zircon grains from the two quartz porphyry samples (ZK809-1 and ZK809-2). The analytical results are shown in Table 1. All the zircon grains analyzed are idiomorphic crystals that are 35–100 μm long. The aspect ratios are approximately 3:1–1:1 (Figure 5). As the U and Th concentrations are exceptionally high (for most of the analysis points, U is $8721\text{--}48,802 \times 10^{-6}$ but can reach $165,623 \times 10^{-6}$; and Th is $819\text{--}13,033 \times 10^{-6}$ but can reach $734,544 \times 10^{-6}$), most of the zircon grains from the two samples display weak zonal structures (Figure 5). Those showing obvious zones yield ages older than 189 Ma, suggesting they are inherited zircons. The Th/U ratio lies mostly in the 0.10–0.38 range, which also points to a magmatic origin. The zircon $^{206}\text{Pb}/^{238}\text{U}$ surface harmonic ages for sample ZK809-1 are 137–140 Ma, and the weighted average age is 138.0 ± 1.1 Ma (MSWD = 0.33; $n = 12$). The $^{206}\text{Pb}/^{238}\text{U}$ surface harmonic ages for sample ZK809-2 are 137–142 Ma, and the weighted average age is 138.6 ± 1.1 Ma (MSWD = 0.49; $n = 15$). Both ages represent the crystallization of the quartz porphyry. Both samples yield older ages (Figure 6A,C) for the inherited zircons.

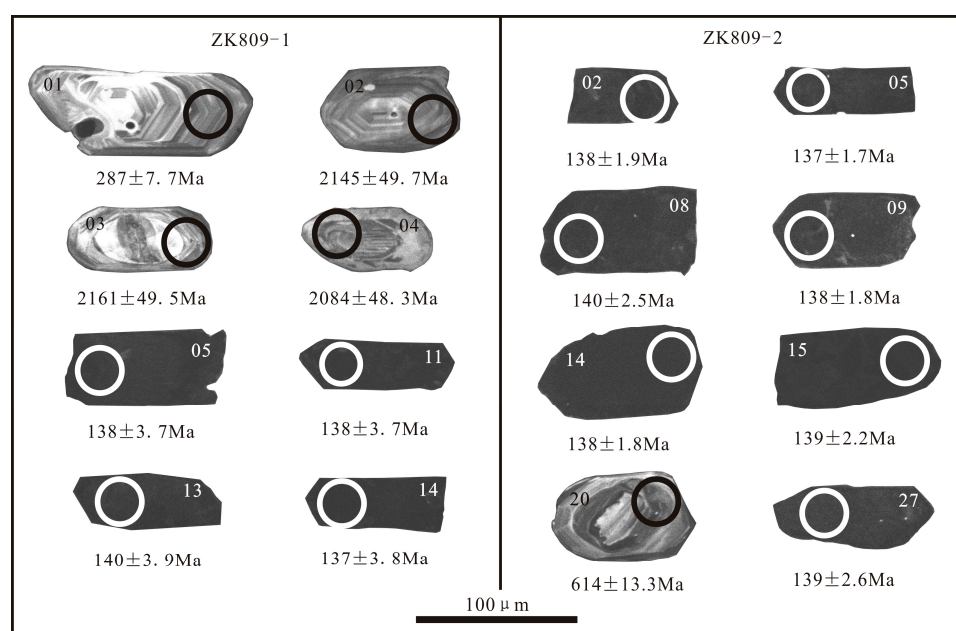


Figure 5. Typical CL images of zircons and analyzed spots from the quartz porphyry in the Weilasituo Sn-polymetallic deposit.

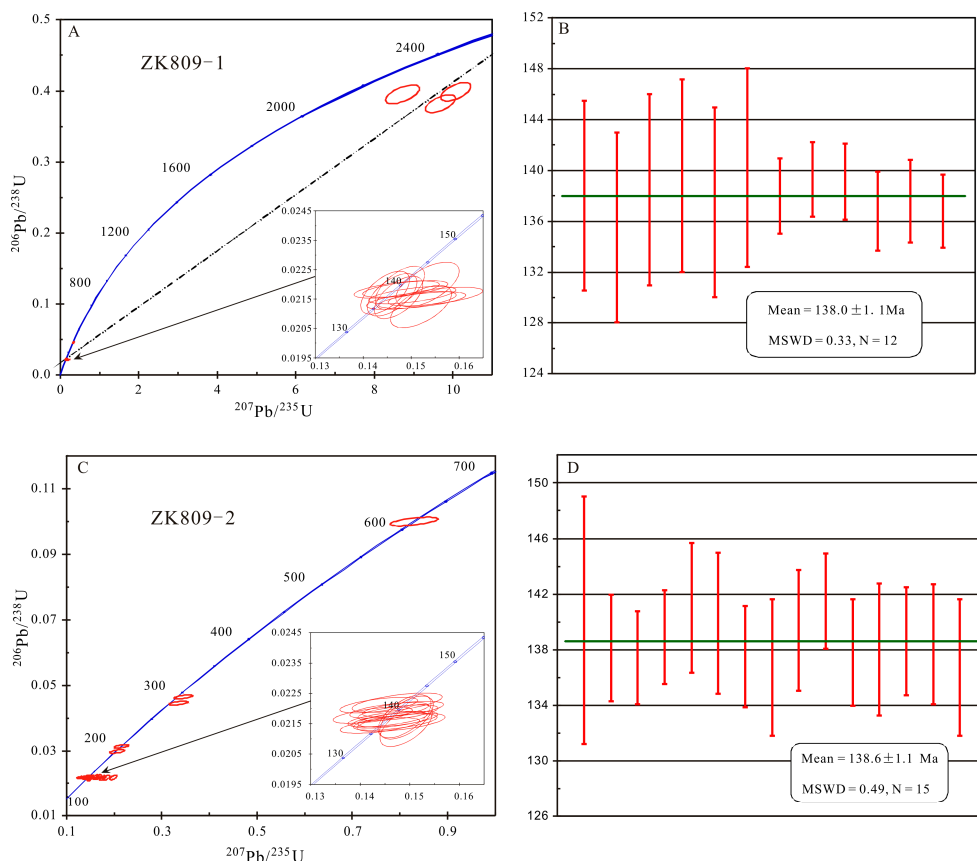


Figure 6. U-Pb Concordia diagram of zircon of quartz porphyry (A,C); weighted mean ages of zircon U-Pb dating for quartz porphyry (B,D).

5.2. Molybdenite Re-Os Geochronology

Table 2 presents the Re-Os isotopic results of nine molybdenite samples from the deposit. The test results indicate that $w(\text{Re}) = 55.2\text{--}712.5$ ng/g, $w(\text{Os}) = 0.152\text{--}9.222$ ng/g, $w(^{187}\text{Re}) = 34.71\text{--}447.80$ ng/g, and $w(^{187}\text{Os}) = 0.0216\text{--}1.041$ ng/g. As the relative concentration of common Os is higher than that of ^{187}Os , the isochron age (135 ± 7 Ma) was interpreted as the formation time of the molybdenite (Figure 7), which indicates that mineralization of the Weilasituo Sn-polymetallic deposit occurred in the early stage of the Early Cretaceous.

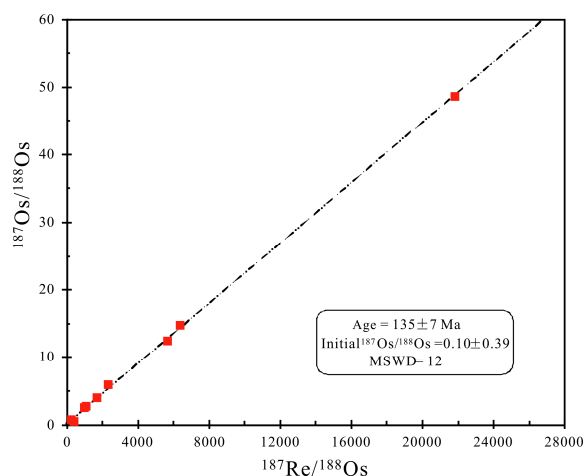


Figure 7. Re-Os isochron ages of quartz porphyry of the Weilasituo Sn-polymetallic deposit.

Table 1. LA-ICP-MS zircon U-Pb dating data of quartz porphyry of Weilasituo deposit.

Sample No.	Th (ppm)	U (ppm)	Th/U	Isotopic Ratios						Ages (Ma)					
				²⁰⁷ Pb/ ²⁰⁶ Pb		²⁰⁷ Pb/ ²³⁵ U		²⁰⁶ Pb/ ²³⁸ U		²⁰⁷ Pb/ ²⁰⁶ Pb		²⁰⁷ Pb/ ²³⁵ U		²⁰⁶ Pb/ ²³⁸ U	
				Ratio	1σ	Ratio	1σ	Ratio	1σ	Ages	1σ	Ages	1σ	Ages	1σ
ZK809-1															
ZK809-1-1	122	323	0.38	0.0508	0.0015	0.3419	0.0128	0.0455	0.0013	230	65	299	10	287	7.7
ZK809-1-2	261	337	0.77	0.16	0.0034	8.7234	0.3532	0.3947	0.0108	2455	36	2310	37	2145	49.7
ZK809-1-3	163	560	0.29	0.1619	0.0032	10.0799	0.3126	0.3982	0.0107	2475	33	2442	29	2161	49.5
ZK809-1-4	101	573	0.18	0.1666	0.0033	9.6905	0.3119	0.3816	0.0104	2524	33	2406	30	2084	48.3
ZK809-1-5	1699	11,150	0.15	0.0653	0.0015	0.1987	0.006	0.0216	0.0006	784	46	184	5	138	3.7
ZK809-1-6	2193	14,821	0.15	0.0482	0.001	0.1461	0.0042	0.0216	0.0006	109	48	138	4	138	3.7
ZK809-1-7	4465	18,362	0.24	0.0543	0.0015	0.1521	0.0052	0.0212	0.0006	384	59	144	5	136	3.7
ZK809-1-8	4961	23,997	0.21	0.052	0.0013	0.1619	0.0052	0.0218	0.0006	286	55	152	5	139	3.8
ZK809-1-9	13,033	47,595	0.27	0.0449	0.0009	0.1446	0.0042	0.0217	0.0006	0.1	0	137	4	139	3.8
ZK809-1-10	5151	27,486	0.19	0.0475	0.001	0.1477	0.0042	0.0219	0.0006	73	48	140	4	140	3.8
ZK809-1-11	12,609	48,802	0.26	0.0488	0.001	0.1474	0.0041	0.0216	0.0006	139	46	140	4	138	3.7
ZK809-1-12	3246	23,933	0.14	0.0556	0.0013	0.1745	0.0055	0.0218	0.0006	437	51	163	5	139	3.8
ZK809-1-13	1568	14,876	0.11	0.0492	0.0014	0.1535	0.0054	0.022	0.0006	158	65	145	5	140	3.9
ZK809-1-14	11,780	51,925	0.23	0.0521	0.0011	0.1579	0.0047	0.0214	0.0006	290	49	149	4	137	3.8
ZK809-1-15	3426	13,869	0.25	0.0487	0.0014	0.1503	0.0074	0.0216	0.0002	134	66	142	7	138	1.5
ZK809-1-16	8656	39,837	0.22	0.0475	0.0013	0.1488	0.0073	0.0218	0.0002	72	65	141	6	139	1.5
ZK809-1-17	8103	36,750	0.22	0.0472	0.0014	0.147	0.0073	0.0218	0.0002	59	67	139	6	139	1.5
ZK809-1-18	5164	25,663	0.2	0.0656	0.0021	0.204	0.0105	0.0211	0.0003	792	65	189	9	135	1.6
ZK809-1-19	2363	12,632	0.19	0.0497	0.0015	0.1501	0.0077	0.0215	0.0003	180	71	142	7	137	1.6
ZK809-1-20	4209	21,271	0.2	0.0528	0.0017	0.1551	0.0081	0.0216	0.0003	321	72	146	7	138	1.6
ZK809-1-21	7071	34,791	0.2	0.0481	0.0013	0.1523	0.0074	0.0215	0.0002	104	64	144	7	137	1.5
ZK809-1-22	1050	11,105	0.09	0.0721	0.0022	0.2256	0.0115	0.0215	0.0003	988	61	207	10	137	1.6
ZK809-2															
ZK809-2-1	1157	10,593	0.11	0.0489	0.0012	0.1487	0.0067	0.022	0.0002	144	57	141	6	140	4.5
ZK809-2-2	3862	21,422	0.18	0.048	0.0011	0.1476	0.0066	0.0217	0.0002	97	56	140	6	138	1.9
ZK809-2-3	7743	26,847	0.29	0.0524	0.0016	0.1685	0.0082	0.0217	0.0002	302	67	158	7	138	2.2
ZK809-2-4	236	694	0.34	0.0547	0.0016	0.3359	0.0163	0.0445	0.0005	400	62	294	12	280	2.7
ZK809-2-5	6779	12,142	0.56	0.0475	0.0014	0.1483	0.0073	0.0215	0.0002	72	71	140	6	137	1.7
ZK809-2-6	5844	34,485	0.17	0.0445	0.0011	0.1426	0.0065	0.0218	0.0002	0	0	135	6	139	1.7

Table 1. Cont.

Sample No.	Th (ppm)	U (ppm)	Th/U	Isotopic Ratios						Ages (Ma)					
				$^{207}\text{Pb}/^{206}\text{Pb}$		$^{207}\text{Pb}/^{235}\text{U}$		$^{206}\text{Pb}/^{238}\text{U}$		$^{207}\text{Pb}/^{206}\text{Pb}$		$^{207}\text{Pb}/^{235}\text{U}$		$^{206}\text{Pb}/^{238}\text{U}$	
				Ratio	1 σ	Ratio	1 σ	Ratio	1 σ	Ages	1 σ	Ages	1 σ	Ages	1 σ
ZK809-2															
ZK809-2-7	4292	22,936	0.19	0.0464	0.0011	0.1438	0.0064	0.0221	0.0002	16	56	136	6	141	2.3
ZK809-2-8	3150	19,105	0.16	0.0481	0.0011	0.1459	0.0065	0.0219	0.0002	102	55	138	6	140	2.5
ZK809-2-9	3506	10,660	0.33	0.0496	0.0014	0.1471	0.0069	0.0216	0.0002	178	62	139	6	138	1.8
ZK809-2-10	5976	37,780	0.16	0.0438	0.0011	0.1333	0.006	0.0216	0.0002	0	0	127	5	138	1.7
ZK809-2-11	1160	4441	0.26	0.0532	0.0014	0.3462	0.0159	0.0464	0.0005	335	57	302	12	292	4.9
ZK809-2-12	734,544	165,623	4.44	0.4377	0.0102	1.8432	0.082	0.0369	0.0004	4044	35	1061	29	233	4.5
ZK809-2-13	6510	30,010	0.22	0.0463	0.0012	0.144	0.0066	0.0214	0.0002	12	59	137	6	137	2.5
ZK809-2-14	7371	35,849	0.21	0.042	0.001	0.1328	0.006	0.0216	0.0002	0	0	127	5	138	1.8
ZK809-2-15	4028	21,700	0.19	0.0488	0.0012	0.1477	0.0066	0.0219	0.0002	137	55	140	6	139	2.2
ZK809-2-16	1251	12,472	0.1	0.0461	0.0015	0.1475	0.0074	0.0222	0.0003	1.7	75	140	7	142	1.7
ZK809-2-17	5697	17,094	0.33	0.047	0.0011	0.1464	0.0066	0.0216	0.0002	50	57	139	6	138	1.9
ZK809-2-18	11.8	610	0.02	0.0462	0.0021	0.2071	0.0128	0.0297	0.0005	10	106	191	11	189	3.5
ZK809-2-19	7.2	242	0.03	0.049	0.0021	0.2164	0.0128	0.0313	0.0004	146	96	199	11	198	5.2
ZK809-2-20	172	802	0.21	0.0615	0.0017	0.8299	0.0411	0.0999	0.0011	656	58	614	23	614	13.3
ZK809-2-21	7783	35,035	0.22	0.0488	0.0012	0.1456	0.0066	0.0217	0.0002	140	56	138	6	138	2.4
ZK809-2-22	2588	15,834	0.16	0.0426	0.001	0.1292	0.0058	0.0218	0.0002	0	0	123	5	139	8.4
ZK809-2-23	1544	9814	0.16	0.0488	0.0011	0.162	0.005	0.0219	0.0006	139.7	51	153	4	139	2.3
ZK809-2-24	4594	11,160	0.41	0.0545	0.0013	0.1766	0.0057	0.0216	0.0006	390	52	165	5	138	2
ZK809-2-25	1478	10,299	0.14	0.0499	0.0011	0.1675	0.0052	0.0219	0.0006	189	52	157	5	140	2.1
ZK809-2-26	4561	25,814	0.18	0.0462	0.001	0.149	0.0044	0.0217	0.0006	9	49	141	4	139	1.9
ZK809-2-27	819	8721	0.09	0.0593	0.0013	0.1993	0.0061	0.0218	0.0006	579	47	185	5	139	2.6
ZK809-2-28	3215	20,693	0.16	0.0461	0.001	0.1494	0.0044	0.0217	0.0006	4	49	141	4	138	2.2
ZK809-2-29	4454	25,173	0.18	0.048	0.001	0.1493	0.0043	0.0214	0.0006	98	49	141	4	137	2.5
ZK809-2-30	5906	30,761	0.19	0.0558	0.0013	0.1846	0.0059	0.0217	0.0006	443	52	172	5	138	2.3

Table 2. Results of Re-Os isotopic analyses of greisen stage from the Weilasituo Sn-polymetallic deposit.

Sample No.	Weight (g)	Re (ppb)		Common Os (ppb)		¹⁸⁷ Re (ppb)		¹⁸⁷ Os (ppb)		¹⁸⁷ Re/ ¹⁸⁸ Os		¹⁸⁷ Os/ ¹⁸⁸ Os	
		Measured	2σ	Measured	2σ	Measured	2σ	Measured	2σ	Measured	2σ	Measured	2σ
ZK809-1	0.01951	552.7	1.6	1.136	0.0039	347.4	1	0.8724	0.0028	2337	23.6	5.852	0.01
ZK809-2	0.0168	491.6	1.4	2.155	0.0069	309	0.9	0.7616	0.0024	1092	11	2.682	0.004
ZK809-3	0.0106	495.8	1.4	9.222	0.2001	311.6	0.9	0.669	0.0125	256.8	6	0.5491	0.0036
ZK809-5	0.0116	306	0.9	1.477	0.0055	192.3	0.6	0.4799	0.0016	998	10.1	2.484	0.004
ZK809-4	0.0106	712.5	2.1	2.011	0.0066	447.8	1.3	1.041	0.0032	1704	17.2	3.954	0.006
IZK02401-2*	0.0497	55.2	0.38	0.698	0.0575	34.71	0.24	0.0216	0.0157	382.1	31.6	0.238	0.174
IZK0403-1*	0.0094	189.5	1.9	0.161	0.0032	119.1	1.2	0.2594	0.007	5677	127	12.36	0.42
IZK0403-3*	0.0289	43.31	0.42	0.033	0.0004	27.22	0.26	0.0627	0.0009	6382	96	14.71	0.28
IZK1501-1*	0.006	685.6	10.1	0.152	0.0018	430.9	6.4	0.9581	0.0122	21854	410	48.59	0.84

Note: * samples from [16].

5.3. Major and Trace Elements

Whole-rock geochemical measurements of quartz porphyry samples from the Weilasituo deposit are shown in Table 3. The samples are rich in silicon, alkalis and aluminum. The analyses indicate SiO_2 , $\text{Na}_2\text{O} + \text{K}_2\text{O}$ and $\text{Na}_2\text{O}/\text{K}_2\text{O}$ ranges of 71.57 wt %–78.60 wt %, 8.85 wt %–10.44 wt %, and 1.37–2.94. Therefore, these rocks belong to the high-K calc-alkaline series (Figure 8A, [53]). The Al_2O_3 values vary from 12.69 wt %–16.32 wt %, the A/CNK values range from 0.94 to 1.21, and the A/NK values range from 1.40 to 1.75, indicating that these samples are high-K calc-alkaline, weakly meta aluminous to peraluminous rocks (Figure 8B; [54]). In the TAS diagram (Figure 8C; [55]), the data points plot within the granite zone; in the $\text{Na}_2\text{O}-\text{K}_2\text{O}$ diagram (Figure 8D; [56]), some of the samples plot within the potassium zone, while the remainder plot within the sodium zone. The quartz porphyry is relatively poor in Mg, with Mg concentrations ranging from 0.09 wt %–0.19 wt %.

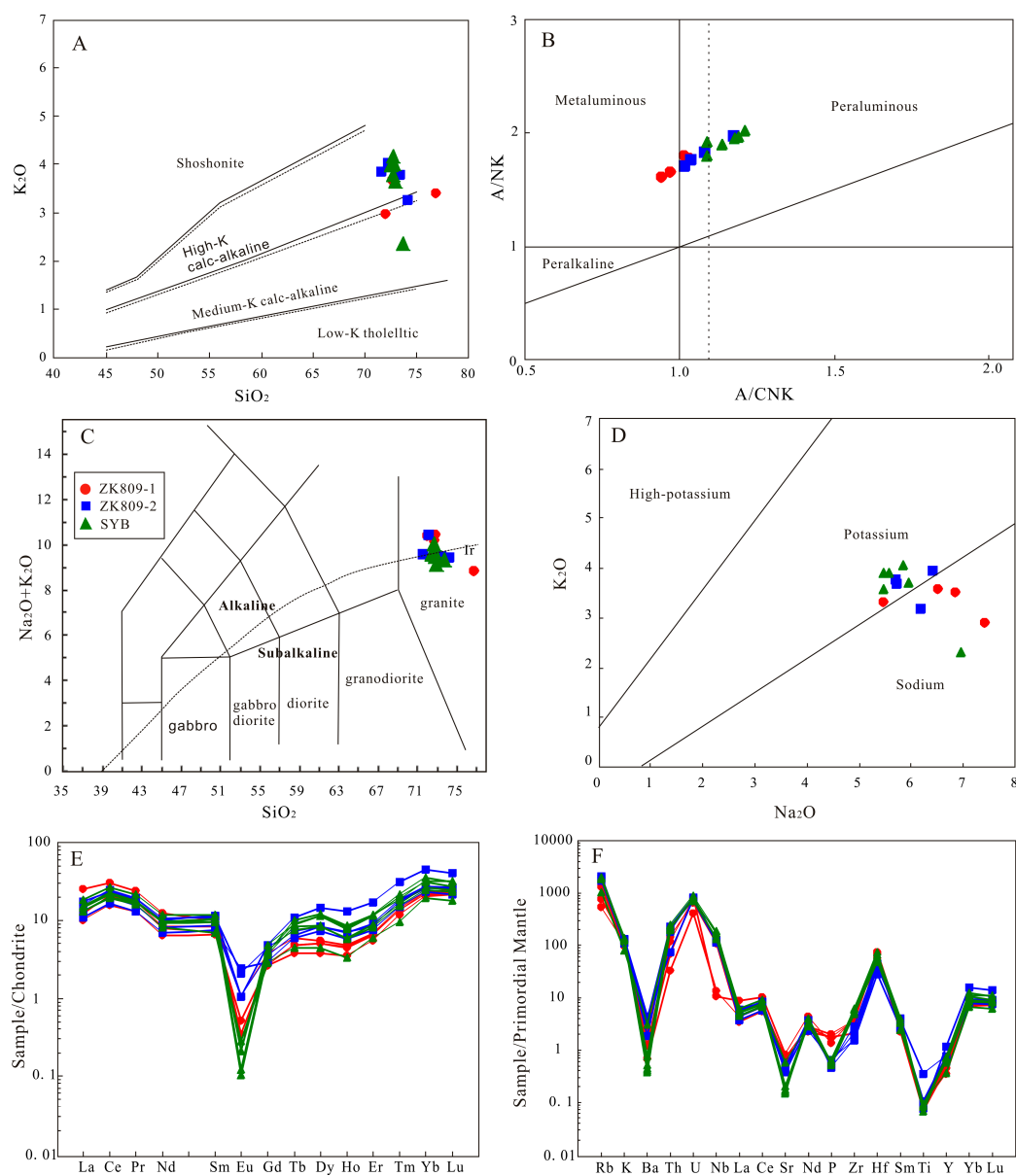


Figure 8. (A) SiO_2 versus $(\text{Na}_2\text{O} + \text{K}_2\text{O})$ diagram (Middlemost, [55]); (B) Na_2O versus K_2O diagram (Middlemost, [56]); (C) SiO_2 versus K_2O diagram (Peccerillo et al. [53]); (D) A/CNK versus A/NK diagram (Manlar and Piccoli, [54]); (E) Chondrite-normalized REE variation (normalized values are from [57]); (F) Primitive mantle-normalized trace element patterns (normalized values are from [58]).

The REE analytical results (Table 3) indicate relatively low total REE contents in the quartz porphyry ($\Sigma\text{REE} = 27.45\text{--}44.75$ ppm). The standard REE chondrite-normalized diagram shows a relatively flat “seagull” pattern (Figure 8E), with light REE (LREE)/heavy REE (HREE) ratios of 1.48–3.91 and $(\text{La}/\text{Yb})_{\text{N}}$ values of 0.37–1.09. The samples are rich in LREEs and poor in HREEs. The samples show distinct negative Eu anomalies ($\delta\text{Eu} = 0.01\text{--}0.46$), suggesting that the magmatic evolution in the provenance involved long-term fractional crystallization with plagioclase as the main mineral phase [59].

On the standard trace element primitive mantle-normalized diagram (Figure 8F), the quartz porphyry samples display similar variations with very low Sr contents (3.09–17.45 ppm) and fairly high Yb contents (3.25–7.64 ppm), suggesting that the provenance pressure was less than 0.8–1.0 GPa [60]. The samples are relatively rich in large-ion lithophile elements (LILEs) such as Rb, Th, U, K as well as the high field strength elements (HFSEs) Hf and Zr and relatively poor in Ba, P, Sr, Ti and Nb, suggesting significant differentiation in the provenance of the quartz porphyry and implying the involvement of subduction zone processes.

5.4. Lu-Hf Isotopes

After zircon LA-ICP-MS U-Pb dating, microscale zircon Lu-Hf isotope analysis was conducted on the quartz porphyry samples from the Weilasituo deposit (ZK809-1 and ZK809-2). The analytical results are shown in Table 4. The zircons in the quartz porphyry have the similar Hf isotopic compositions. The $^{176}\text{Hf}/^{177}\text{Hf}$ and $\epsilon_{\text{Hf}}(t)$ values at the 25 measuring points are 0.282742–0.282882 and 1.90–6.90, respectively. The $\epsilon_{\text{Hf}}(t)$ isotopic calculations all plot between the chondritic meteorite and depleted mantle evolution lines (Figure 9B), as well as in the Phanerozoic igneous region of the eastern Central Asian Orogen (Figure 9A). The gray figures are quoted from [20,61,62]. At all the analysis points, T_{DM2} vary from 1069 to 747 Ma. As the zircon $f_{\text{Lu}/\text{Hf}}$ value is substantially lower than that in felsic crust (0.72, [63]) and mafic crust (0.34, [64]) and the T_{DM2} is close to the age of the source materials retained in the crust, the result indicates that the quartz porphyry magma originated from lower crustal materials.

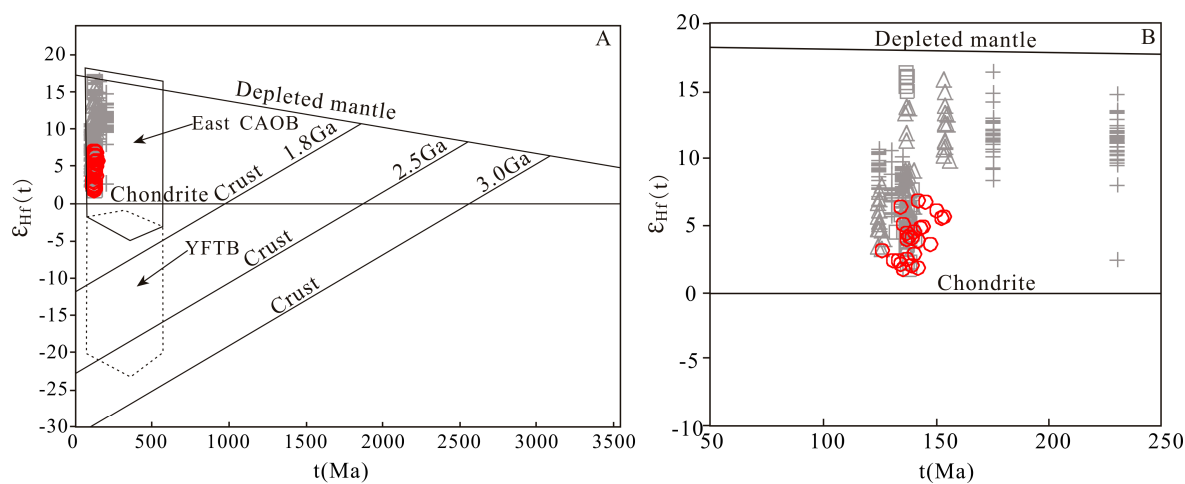


Figure 9. Variations of $\epsilon_{\text{Hf}}(t)$ versus crystallization age of zircons (A,B) of the Weilasituo Sn-polymetallic deposit. The gray areas of granite is quoted from [20,61,62].

Table 3. Major (wt %) and trace elements (ppm) data of quartz porphyry from the Weilasituo Sn-polymetallic deposit.

Sample No.	ZK809-1-1	ZK809-1-2	ZK809-1-3	ZK809-1-4	ZK809-2-1	ZK809-2-2	ZK809-2-3	ZK809-2-4	SYB-01*	SYB-02*	SYB-03*	SYB-04*	SYB-05*	SYB-06*
Rock Type	Quartz Porphyry													
SiO ₂	72.84	76.8	72.67	72.01	73.4	72.15	71.57	74.15	73.69	72.68	72.91	72.79	72.52	72.76
Al ₂ O ₃	14.63	12.69	15.63	16.16	15.09	15.42	16.32	14.43	15.54	16.04	15.93	16.12	16.15	15.63
TiO ₂	0.016	0.018	0.015	0.015	0.076	0.023	0.016	0.023	0.020	0.019	0.014	0.018	0.017	0.02
Fe ₂ O ₃	1.09	0.79	0.70	0.83	0.53	0.50	0.59	0.55	0.305	0.46	0.795	0.51	0.654	0.526
FeO	0.90	0.67	0.58	0.72	0.45	0.43	0.50	0.47	0.26	0.39	0.61	0.43	0.55	0.47
MnO	0.043	0.029	0.022	0.014	0.047	0.042	0.06	0.056	0.018	0.027	0.036	0.021	0.04	0.027
MgO	0.11	0.12	0.15	0.15	0.16	0.19	0.18	0.11	0.12	0.083	0.192	0.148	0.098	0.159
CaO	0.205	0.224	0.256	0.29	0.27	0.16	0.17	0.13	0.151	0.104	0.118	0.124	0.103	0.113
Na ₂ O	6.84	5.46	6.51	7.42	5.71	6.4	5.70	6.18	6.95	5.95	5.46	5.46	5.57	5.85
K ₂ O	3.6	3.39	3.66	2.96	3.78	4.04	3.86	3.26	2.36	3.79	3.65	4.00	3.99	4.16
P ₂ O ₅	0.029	0.037	0.039	0.043	0.01	0.014	0.012	0.011	0.014	0.013	0.012	0.012	0.012	0.011
LOI	0.65	0.47	0.30	0.20	0.14	0.31	0.35	0.19	0.32	0.34	0.37	0.29	0.34	0.24
Total	100.94	100.7	100.53	100.8	99.66	99.68	99.33	99.6	99.75	99.9	100.1	99.92	100.04	99.97
Na ₂ O + K ₂ O	10.44	8.85	10.17	10.38	9.49	10.44	9.56	9.44	9.31	9.74	9.11	9.46	9.56	10.01
Na ₂ O/K ₂ O	1.90	1.61	1.78	2.51	1.51	1.58	1.48	1.90	2.94	1.57	1.50	1.37	1.40	1.41
La	6.02	2.93	2.37	2.77	3.75	2.57	4.13	2.98	3.10	3.63	3.58	3.08	4.30	3.43
Ce	18.28	11.72	9.60	12.86	14.98	10.10	14.27	12.00	11.80	13.70	13.50	12.10	16.30	13.20
Pr	2.28	1.52	1.23	1.65	1.83	1.24	1.79	1.48	1.51	1.71	1.71	1.59	2.06	1.66
Nd	5.83	3.72	2.99	3.86	4.97	3.20	4.73	3.79	3.78	4.50	4.45	4.29	5.43	4.26
Sm	1.55	1.06	1.00	1.27	1.65	1.15	1.75	1.30	1.06	1.47	1.57	1.60	1.79	1.46
Eu	0.06	0.03	0.03	0.02	0.12	0.14	0.06	0.06	0.016	0.012	0.007	0.006	0.012	0.006
Gd	0.75	0.53	0.54	0.57	0.91	0.59	0.99	0.72	0.58	0.839	0.806	0.785	0.975	0.73
Tb	0.22	0.14	0.18	0.18	0.27	0.22	0.41	0.24	0.165	0.282	0.338	0.37	0.329	0.31
Dy	1.40	0.97	1.28	1.28	2.10	1.84	3.64	2.12	1.12	2.09	2.87	3.05	2.89	2.15
Ho	0.27	0.20	0.26	0.25	0.40	0.33	0.73	0.39	0.189	0.334	0.431	0.483	0.453	0.322
Er	1.13	0.90	1.08	1.05	1.39	1.24	2.78	1.50	0.968	1.45	1.89	1.92	1.92	1.33
Tm	0.36	0.30	0.34	0.34	0.44	0.38	0.80	0.47	0.24	0.409	0.499	0.543	0.467	0.387
Yb	3.95	3.44	3.62	3.85	4.36	3.90	7.64	4.63	3.25	4.47	5.24	6.02	5.35	4.21
Lu	0.62	0.54	0.56	0.59	0.65	0.55	1.03	0.68	0.456	0.628	0.684	0.796	0.813	0.589
Y	2.45	1.61	2.05	2.00	3.50	2.70	5.22	3.48	1.68	2.75	3.33	3.35	3.18	2.60
∑REE	42.72	28.00	25.08	30.54	37.82	27.45	44.75	32.36	28.23	35.524	37.575	36.633	43.089	34.044
LREE	34.02	20.98	17.22	22.43	27.30	18.40	26.73	21.61	21.27	25.02	24.82	22.67	29.89	24.02
HREE	8.70	7.02	7.86	8.11	10.52	9.05	18.02	10.75	6.97	10.5	12.76	13.97	13.2	10.03
LREE/HREE	3.91	2.99	2.19	2.77	2.60	2.03	1.48	2.01	3.05	2.38	1.95	1.62	2.27	2.39
δEu	0.15	0.11	0.11	0.06	0.27	0.46	0.13	0.17	0.06	0.03	0.02	0.01	0.03	0.02
(La/Yb) _N	1.09	0.61	0.47	0.52	0.62	0.47	0.39	0.46	0.68	0.58	0.49	0.37	0.58	0.58
Li	1200	811	556	405	388	347	650	496	287	374	512	274	569	365
Be	5.54	4.57	5.83	5.94	5.20	5.45	5.32	5.19	5.05	4.73	5.08	4.22	4.99	5.17
Sc	2.82	2.42	2.63	2.02	3.52	2.87	2.67	3.08	1.64	1.73	1.89	2.43	2.26	1.92

Table 3. Cont.

Sample No.	ZK809-1-1	ZK809-1-2	ZK809-1-3	ZK809-1-4	ZK809-2-1	ZK809-2-2	ZK809-2-3	ZK809-2-4	SYB-01*	SYB-02*	SYB-03*	SYB-04*	SYB-05*	SYB-06*
Rock Type	Quartz Porphyry													
Cr	6.10	9.23	4.29	10.59	9.01	9.59	3.39	4.32	5.23	1.07	2.32	2.08	2.17	1.16
Co	0.08	0.40	0.78	4.81	2.03	1.18	1.40	1.65	0.45	0.14	0.33	0.14	0.19	0.14
Ni	2.59	1.67	5.02	6.02	3.39	2.85	3.07	2.88	4.11	0.39	1.50	0.90	0.99	0.30
Ga	68.2	70.4	69.5	67.6	64.0	68.7	65.0	64.6	76.2	73.9	72.4	75.0	76.1	75.7
Rb	476	339	1012	819	1200	1200	1300	1100	651	1157	1153	1233	1262	1192
Sr	17.45	14.77	13.95	14.36	9.92	9.43	9.47	7.81	12.40	3.34	4.22	3.35	3.09	3.63
Ba	8.37	4.80	8.54	16.65	13.10	30.7	26.78	26.62	21.70	3.62	3.12	2.68	5.31	2.84
U	17.3	8.7	15.5	13.4	16.6	15.9	14.6	17.5	14.8	16.2	15.8	18.6	17.1	15.1
Th	5.9	2.8	9.8	11.9	15.6	6.3	16.9	19.1	19.7	17.9	16.7	20.9	17.7	17.0
Nb	77.5	97.7	76.9	76.3	87.9	90.0	79.8	86.1	95.1	102	127	133	119	126
Ta	0.9	0.5	2.7	2.4	28.1	26.2	30.1	32.42	26.3	32.9	41.4	46.4	40.7	34.8
Zr	43.9	39.4	23.2	39.4	17.8	16.8	23.7	32.3	66.3	55.2	59.1	65.7	69.9	54.1
Hf	22.5	20.8	17.1	21.0	11.9	8.8	13.8	13.6	22.8	15.6	17.8	18.0	20.2	14.9
DI	95.06	97.41	96.39	96.19	94.91	96.22	93.68	97.07	96.97	96.26	94.47	95.28	95.27	96.50
A/CNK	0.943	0.972	1.033	1.014	1.08	1.015	1.177	1.036	1.09	1.139	1.212	1.191	1.181	1.091
A/NK	1.40	1.43	1.54	1.56	1.59	1.48	1.71	1.53	1.67	1.65	1.75	1.70	1.69	1.56
SI	0.88	1.15	1.29	1.24	1.47	2.45	2.51	1.03	1.20	0.78	1.79	1.40	0.90	1.42
AR	5.75	5.36	4.56	4.42	4.23	5.06	3.76	4.69	3.92	4.04	3.63	3.79	3.86	4.49
R1	1523	2339	1635	1419	1945	1562	1817	1961	1883	1827	2032	1956	1893	1774
R2	313	278	341	353	334	335	355	304	329	331	336	338	334	327
A/MF	4.96	5.61	7.46	6.57	6.99	6.64	6.42	8.00	14.63	11.87	6.73	9.85	8.67	8.98
C/MF	0.13	0.18	0.22	0.21	0.23	0.13	0.12	0.13	0.26	0.14	0.09	0.14	0.1	0.12
Tzr	672	674	638	670	626	616	649	662	717	706	717	723	727	701
Zr/Hf	1.95	1.89	1.36	1.88	1.50	1.92	1.71	2.38	2.91	3.54	3.32	3.65	3.46	3.63
Nb/Ta	86.11	195.40	28.48	31.80	3.13	3.43	2.65	2.65	3.62	3.10	3.07	2.87	2.92	3.62
Y/Ho	9.07	8.05	7.88	8.00	8.75	8.18	7.15	8.92	8.89	8.23	7.72	6.93	7.01	8.07

Note: * samples from [17].

Table 4. Zircon Hf isotopic composition for zircons from quartz porphyry from the Weilasituo Sn-polymetal deposit.

Sample No.	^{176}Yb	^{176}Lu	2σ	^{176}Hf	2σ	I_{Hf}	$\hat{a}_{\text{Hf}}(0)$	$\hat{a}_{\text{Hf}}(t)$	T_{DM}	T_{DMc}	$f_{\text{Lu/Hf}}$
	^{177}Hf	^{177}Hf		^{177}Hf							
ZK809-1											
ZK809-1-5	0.14894	0.004678	0.000011	0.282894	0.00003	0.282882	4.32	7	562	747	−0.86
ZK809-1-6	0.070153	0.002193	0.000011	0.282827	0.000033	0.282822	1.96	4.91	621	883	−0.93
ZK809-1-8	0.094014	0.002688	0.00013	0.282759	0.000034	0.282753	−0.44	2.28	731	1045	−0.92
ZK809-1-11	0.119131	0.003901	0.00006	0.282757	0.000029	0.282747	−0.52	2.16	759	1053	−0.88
ZK809-1-12	0.099831	0.003076	0.00011	0.282794	0.000046	0.282787	0.78	3.3	687	973	−0.91
ZK809-1-13	0.058014	0.001766	0.000017	0.282821	0.000016	0.282816	1.73	4.57	624	899	−0.95
ZK809-1-14	0.23863	0.007394	0.000128	0.28278	0.000028	0.282762	0.29	2.53	806	1025	−0.78
ZK809-1-16	0.208726	0.006686	0.00006	0.282781	0.000027	0.282763	0.3	2.69	787	1018	−0.8
ZK809-1-17	0.187535	0.00576	0.000021	0.282887	0.000025	0.282873	4.07	6.52	592	773	−0.83
ZK809-2											
ZK809-2-1	0.068173	0.002062	0.000087	0.282811	0.000039	0.282805	1.37	4.23	643	921	−0.94
ZK809-2-2	0.204887	0.00609	0.000197	0.282841	0.000021	0.282825	2.43	5.03	674	876	−0.82
ZK809-2-7	0.08257	0.002656	0.000066	0.282884	0.000022	0.282877	3.97	6.9	545	756	−0.92
ZK809-2-8	0.101062	0.003427	0.000041	0.28285	0.000019	0.28284	2.77	5.77	609	834	−0.9
ZK809-2-10	0.225517	0.007277	0.000082	0.282789	0.00003	0.28277	0.59	3	788	1002	−0.78
ZK809-2-13	0.089718	0.002885	0.000107	0.282749	0.000024	0.282742	−0.81	2.05	750	1065	−0.91
ZK809-2-14	0.151158	0.004783	0.000067	0.28283	0.000035	0.282817	2.04	4.67	666	896	−0.86
ZK809-2-16	0.055678	0.0018	0.000027	0.282792	0.000014	0.282787	0.7	3.75	666	959	−0.95
ZK809-2-17	0.11063	0.003649	0.000132	0.282849	0.000024	0.282838	2.71	5.67	615	840	−0.89
ZK809-2-23	0.062346	0.002142	0.000029	0.282862	0.000034	0.282856	3.18	6.27	570	801	−0.94
ZK809-2-24	0.055027	0.00173	0.000045	0.282813	0.000017	0.282808	1.44	4.31	635	917	−0.95
ZK809-2-25	0.060326	0.001936	0.000013	0.282804	0.000014	0.282799	1.15	4.06	651	935	−0.94
ZK809-2-26	0.054206	0.001611	0.000031	0.282765	0.00003	0.282761	−0.24	2.54	701	1026	−0.95
ZK809-2-27	0.0481	0.001494	0.000018	0.282807	0.000016	0.282803	1.24	4.12	639	928	−0.95
ZK809-2-28	0.089327	0.00277	0.000015	0.282844	0.000018	0.282837	2.54	5.27	607	854	−0.92
ZK809-2-29	0.116556	0.00372	0.000267	0.282751	0.00004	0.282742	−0.74	1.9	765	1069	−0.89

6. Discussion

6.1. Magmatic-Metallogenic Age Context

The determination of the precise age of mineralization and closely associated intrusions is essential for understanding genetic processes and locating economic deposits [65,66]. Presently, several high-precision and accurate isotopic dating methods exist to determine petrogenetic and metallogenic ages, such as zircon U-Pb [16,25], molybdenite Re-Os [16,25], and cassiterite U-Pb dating [17].

The zircon LA-ICP-MS U-Pb ages we obtained are 138.0 ± 1.1 Ma and 138.6 ± 1.1 Ma, which agree with the zircon U-Pb age of the quartz porphyry (138 ± 2 Ma and 135.7 ± 0.9 Ma) and the cassiterite age of the disseminated mineralization (138 ± 6 Ma) obtained by previous studies [16,17]. In addition, the molybdenite Re-Os isochron age (135 ± 7 Ma) we obtained also agrees with the molybdenite Re-Os isochron age (135 ± 11 Ma), and the cassiterite U-Pb age of the vein-like mineralization (135 ± 6 Ma) obtained by previous studies. Taking into account previous findings, we assume a petrogenetic age range of 138.0–138.6 Ma, which coincides with the age of the disseminated mineralization (138 ± 6 Ma). The vein-like mineralization formed at 135 ± 7 Ma, which was slightly later than the disseminated mineralization. These results indicate that the petrogenesis, as well as the metallogenesis, of the deposit occurred during the early Early Cretaceous. The petrogenetic ages of the various deposits found in the area have been widely examined and summarized over the past years. The results mostly correspond to the Mid-Triassic, Early to middle Jurassic and Early Cretaceous [67], with the Early Cretaceous becoming the most prevalent age. The Early Cretaceous deposits include more hydrothermal Pb-Zn-Ag (Sn-Cu), skarn-type Pb-Zn-Ag (Sn-Fe) and porphyry-type Cu-Mo deposits than porphyry-type Sn (W) deposits.

The study area lies at the eastern end of the Central Asian Orogen, which is sandwiched between the North China Block and the Siberian Plates. The study area was influenced by the evolution and closure of the Paleo-Asian Ocean during the Paleozoic and by the circum-Pacific tectonic domain from the Mesozoic to the Cenozoic [27,68]. Many studies have disconnected the magmatism of late Mesozoic in the SGXR from the subduction of the Pacific Plate [4,69], however, it is evident that the Early Cretaceous magmatism occurred throughout East China. This evidence suggests that the geodynamics underlying the formation of granite during this period must be taken into account. We believe the Pacific Plate played an important role in this magmatism [70]. During the Early Cretaceous, northern China is thought to have experienced a post-orogenic extensional collapse, an environment of post-arc extension closely followed by the subduction of the Paleo-Pacific Plate [26,71–73]. In the Nb-Y tectonic discrimination diagram, the sample points plot within the volcanic arc + syn-collisional granite fields (Figure 10C). In the Rb-Y + Nb diagram, the sample points are all distributed within the syn-collisional granite field (Figure 10D).

As discussed above, we have dated the petrogenesis and metallogenesis of the Weilasituo deposit to the early stage of the Early Cretaceous and conclude that the deposit was affected by the Early Cretaceous compression associated with the Paleo-Pacific Plate.

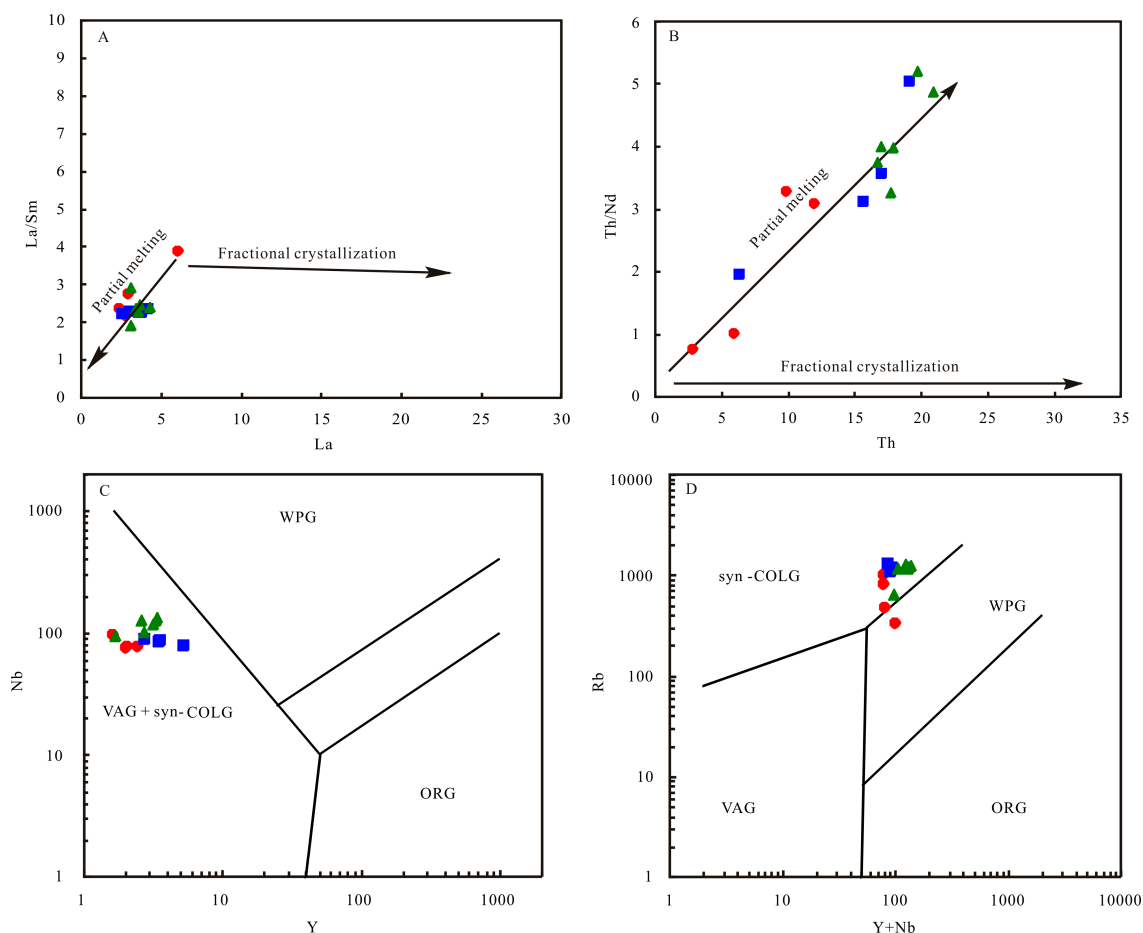


Figure 10. (A) La versus La/Sm diagram (Yang et al. [62]); (B) Th versus Th/Nd diagram (Schiano et al. [74]) (C) Y versus Nb diagram (Pearce et al. [75]); (D) Y + Nb versus Rb diagram (Pearce et al. [75]). Same symbols as Figure 8.

6.2. Petrogenesis and Magma Source

It is of great significance to determine the genetic type of granitoids so that one can understand the magma source, magmatism, and tectonic setting [75,76]. According to the $(Zr + Nb + Ce + Y)\text{-FeO}^T/\text{MgO}$ diagram (Figure 11A) and the $\text{SiO}_2\text{-FeO}^T/\text{MgO}$ diagram (Figure 11B), the quartz porphyry from the Weilasituo deposit exhibit no characteristics of A-type granites. In addition, the rocks are rich in silica (average $\text{SiO}_2 = 73.07$ wt %) and alkalis (average $\text{Na}_2\text{O} + \text{K}_2\text{O} = 9.71$ wt %) with $\text{Na}_2\text{O}/\text{K}_2\text{O}$ ratios from 1.37 to 2.94, Al_2O_3 from 12.69 wt % to 16.32 wt %, and A/CNK ratios from 0.94 to 1.21. These features are typical of high-K calc-alkaline peraluminous granite. The low MgO content (<0.3 wt %) is also indicative of S-type granites [77].

In all the samples, the P-contents of quartz porphyry is very low (0.010%–0.043%) and P_2O_5 decreases with increasing SiO_2 (Figure 11C), while Th increases with Rb (Figure 11D), both of which are important gauges for discriminating I-type granites [77]. The Nb/Ta ratios of the quartz porphyry mostly range from 2.65 to 3.62 (<5) in Table 3, which is a sign of differentiation of peraluminous granite [78]. In the Nb-Nb/Ta diagram and Ta-Nb/Ta diagram (Figure 12A,B), the degree of differentiation of the quartz porphyry samples reaches more than 90%. The Zr/Hf ratios of quartz porphyry range from 1.36 to 3.65 (<25), and the U and Th concentrations are high in zircon, which are typical features of highly differentiated granite [79]. In the Zr-Zr/Hf diagram (Figure 12C), the ratio of Zr/Hf decreases with decreasing Zr content. In the Nb-Y/Ho diagram (Figure 12D), the Y/Ho ratio decreases with the increasing Nb content. The above two characteristics are typical of highly differentiated granite [80]. Additionally, the relatively low total REE contents, the relatively

flat “seagull” pattern in the standard REE chondrite-normalized diagram (Figure 8E), the relatively abundant LREEs with LREE/HREE ratios of 1.48–3.91 (suggesting distinct differentiation), the very low contents of Sr (<400 ppm), the high contents of Yb (>2 ppm), $(La/Yb)_N = 0.37–1.09$, the intensely negative Eu anomalies ($\delta Eu = 0.01–0.46$, Figure 8F) and the relatively high abundances of the LILEs Rb, U, Th, and K compared to the relatively low abundances of Ba, P, Sr, Ti are all indicative of a highly differentiated I-type granite [81].

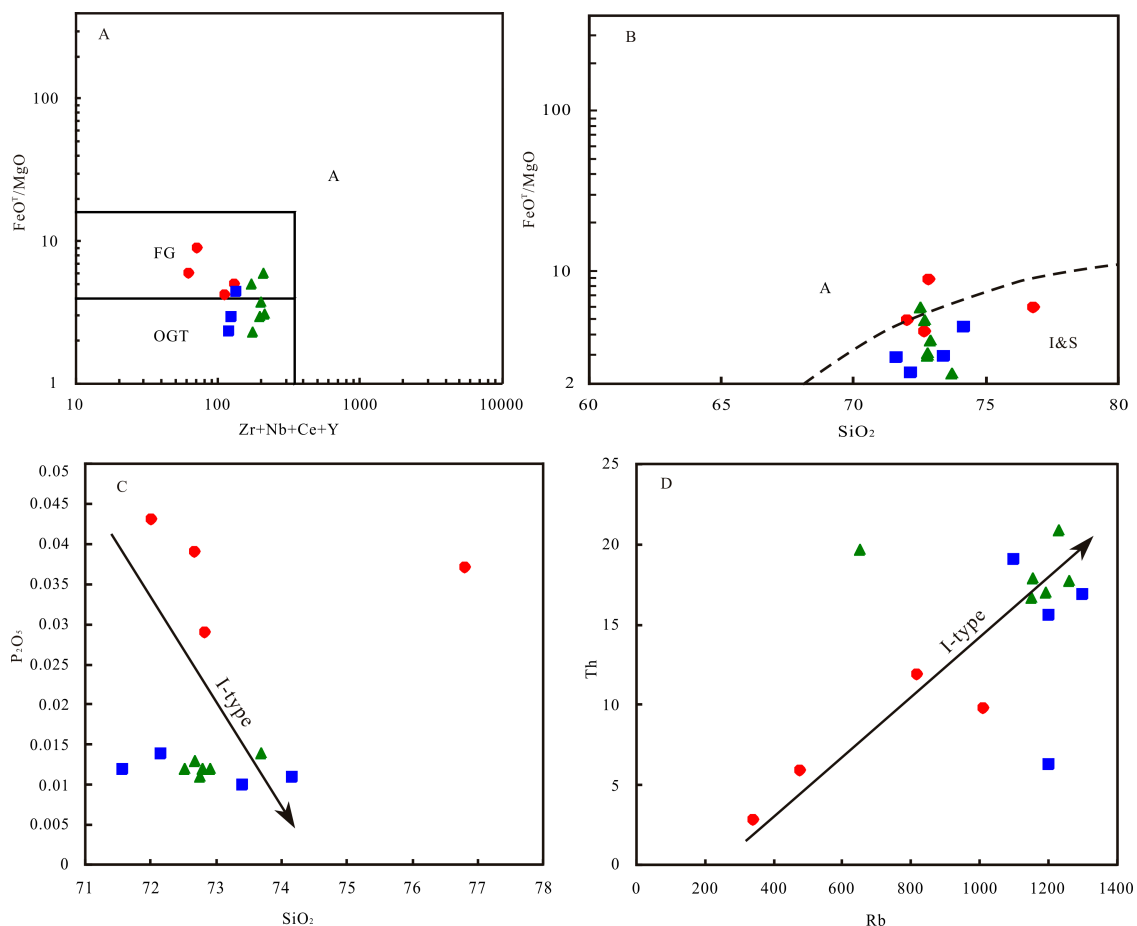


Figure 11. (A) Zr + Nb + Ce + Y versus FeO^T/MgO diagram (Whalen et al. [81]); (B) SiO_2 versus FeO^T/MgO diagram (Eby et al. [82]); (C) SiO_2 versus P_2O_5 diagram; (D) Rb versus Th diagram. Same symbols as Figure 8. FG—fractionated I-type granite; OGT—unfractionated I, S and M type granite; A—A-type granite; I—I-type granite; S—S-type granite.

Overall, we assume that the metallogensis-related quartz porphyry in the deposit is a peraluminous, high-K calc-alkaline I-type granite as previously stated by Wang et al. [17].

Using the bulk rock Zr composition to represent the melt composition (Table 3) in the model of Watson and Harrison [83], zircon-saturation temperatures (T_{Zircon}) were calculated for the quartz porphyry of the Weilasituo deposit. The T_{Zircon} of the quartz porphyry ranges from 616° to 727° (averaging 678°), thus corresponding to a low T_{Zircon} value. In general, highly fractionated granitic magmas generally feature high primary temperatures or large amounts of various volatiles during the later stage. Although the T_{Zircon} of the quartz porphyry is low, the hydrothermal fluid of the Weilasituo deposit was characterized by high-Na, high-F contents [17], which would have been favorable for the differentiation of the quartz porphyry. In addition, volatiles in the residual melt, such as H_2O , Li, F, and Cl, tend to increase with crystallization [84], thus promoting the differentiation of magma.

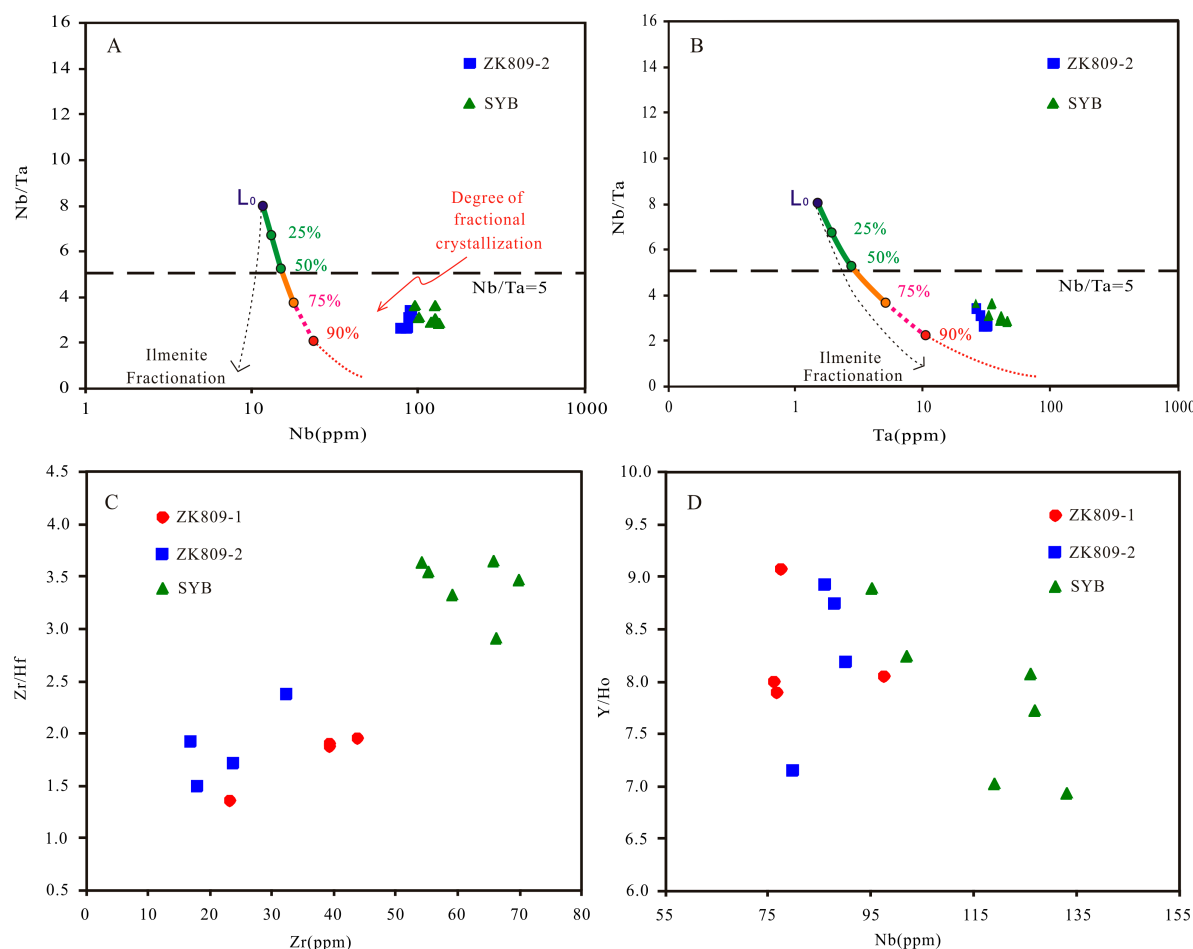


Figure 12. (A) Nb versus-Nb/Ta diagram (Ballouard et al. [78]); (B) Ta versus Nb/Ta diagram (Ballouard et al. [78]); (C) Zr versus Zr/Hf diagram; (D) Nb versus Y/Ho diagram.

Partial melting test results for common crustal rocks have revealed that this type of granite can be produced by the partial melting of water-bearing calc-alkaline to high-K calc-alkaline rocks, and mafic to intermediate metamorphic rocks in the earth's crust. In theory, granitoids can form in many ways, including assimilation-fractional crystallization, magma mixing, or melting of the lower crust [85]. Magma mixing generates supercooled particles and magmatic inclusions [86]. However, no dioritic inclusions were found in the Weilasituo granites. Hence, the granites did not experience significant magma mixing. The zircons from the Weilasituo granites yield $^{206}\text{Pb}/^{238}\text{U}$ ages that are younger than 200 Ma and Th/U values that are greater than 0.1. These data suggest that the zircons were not inherited as a result of contamination by the surrounding host rocks or assimilation. Furthermore, the La-La/Sm diagram (Figure 10A) and the Th-Th/Nd diagram (Figure 10B) also illustrate the presence of partially melted magma in the quartz porphyry from the deposit. All these findings confirm that partial melting controlled the formation of the magma [87].

The Hf isotope composition of the Late Cretaceous granite in this area is summarized. The Hf isotope composition is the same as that of other rocks from the same era, suggesting that these rocks shared the same magma source. The $\varepsilon_{\text{Hf}}(t)$ value of the rock is positive, and the T_{DM2} model ages are 1069–747 Ma, and thus exhibit a large range. Therefore, the materials in the source region mainly came from the juvenile lower crust with some degree of mixing with mantle source materials, which is consistent with the conclusions based on the Sr-Nd isotope [17].

These data suggest that the subduction of the Pale–Pacific Plate caused the lower crust to thicken and delaminate. The delaminated material then entered the underlying mantle, where it partially

melted. As the resulting magma ascended, it reacted with the mantle before intruding into the shallow crust and solidifying in the form of the quartz porphyry.

6.3. Metallogenic Implications

Because the mineralization of the deposit occurred after the intrusion of the quartz porphyry, the mineralization had an inherently close genetic, spatial and temporal relationship with the quartz porphyry [17]. Thus, the ore-forming fluids of Sn-polymetallic mineralization were derived from the highly differentiated quartz porphyry.

Sn, W and Rb are highly incompatible elements. These elements are much more abundant in the crust than in the mantle [88]. Partial melting can lead to the enrichment of these elements in the presence of favorable complexing agents [89].

Chen et al. [90] and Chen and Fu [91] discussed the mechanism of granitic magma formation via the partial melting of thickened lower crust and established three models. (1) During a major period of continent orogenic movement, the strong collision between continental plates compresses and shortens the crust, resulting in thickening and shearing of the lower crust. The temperature rise caused by the thickening of the lower crust and the heat generated by tectonic shearing may lead to partial melting of the lower crust, potentially assisted by the addition of external fluids. (2) After the main orogenic movement, the crust is in the state of tectonic decompression, which affects the thickening of the crust. This process leads to the dehydration of water-bearing minerals, and the addition of these fluids causes the partial melting of the crust. (3) After the main orogenic movement, gravitational instability results in lithospheric delamination of over-thickened crust results in mantle upwelling and the under-plating of the lower crust. These events cause partial melting of the lower crust.

At least in the late Mesozoic, the Great Xing'an Range had the characteristics of a post-collisional environment from the existing paleomagnetic evidence [92]. In recent years, studies in this region have found mafic granulite xenoliths and mafic-ultramafic cumulate xenoliths from the Early Mesozoic (based on ^{40}Ar - ^{39}Ar ages, whole-rock K-Ar isochron ages, and Rb-Sr whole-rock isochron ages in a range of 220 to 237 Ma) and the late Mesozoic (based on zircon U-Pb ages in a range of 120 to 140 Ma). These rocks are believed to be the result of both upwelling and asthenospheric underplating [93]. Therefore, we believe that the granites associated with the Weilasituo are the result of the third mechanism discussed above.

Based on geochronological and geochemical research on the intermediate-acidic intrusive rocks exposed in the area and given the deposit geology and regional tectonics, we assume the following diagenetic and metallogenic dynamic processes. From the Late Jurassic to the Early Cretaceous, the subduction of the Paleo-Pacific Ocean caused the lower crust to thicken and delaminate. The delaminated material then entered the underlying mantle, where it partially melted. The roof of a magma chamber can become enriched in Sn, W, Mo and other elements by convection-driven thermogravimetric diffusion [94]. During the subsequent ascent of this magma, a portion mixed with remelted old crust and became calc-alkaline magma, which rose to the shallow crust and was emplaced in weak locations resulting from local extension, corresponding to the quartz porphyry emplacement. This process caused the ore minerals, Sn in particular, to leach out of the quartz porphyry (Figure 13A). During 138–135 Ma, due to the local extension, fractures and faults developed in the surrounding rocks above the quartz porphyry, and these fractures acted as conduits for the continuous upward migration of fluid. The increase in fluid pressure eventually exceeded the lithostatic pressure of the surrounding rocks, leading to cryptoexplosion and the formation of the breccia pipe. After the emplacement of the quartz porphyry, a large amount of metal-rich magmatic volatiles were released (Figure 13B). Because the magma was rich in Cl and F, Sn tends to migrate in the form of SnCl_2 . The high F activity in the magma lowers the viscosity and enables the segregation of a less viscous, highly enriched residual fluid [95]. At approximately 135 Ma, ore-bearing hydrothermal fluid passed through the fractures, cleavages, and faults, and reacted with the surrounding rocks ("Xilin hot complex") as follows: $\text{SnCl}_2 + 3(\text{Na,K})\text{AlSi}_3\text{O}_8 + 2\text{H}_2\text{O} \rightarrow \text{SnO}_2(\text{cassiterite}) + \text{KAl}_3\text{Si}_3\text{O}_{10}(\text{OH})_2 + 6\text{SiO}_2 + 2\text{NaCl}$

+ H₂. Sn crystallized as cassiterite and was accompanied by the precipitation of other metallogenic elements. These processes formed the Weilasituo Sn-polymetallic deposit (Figure 13C).

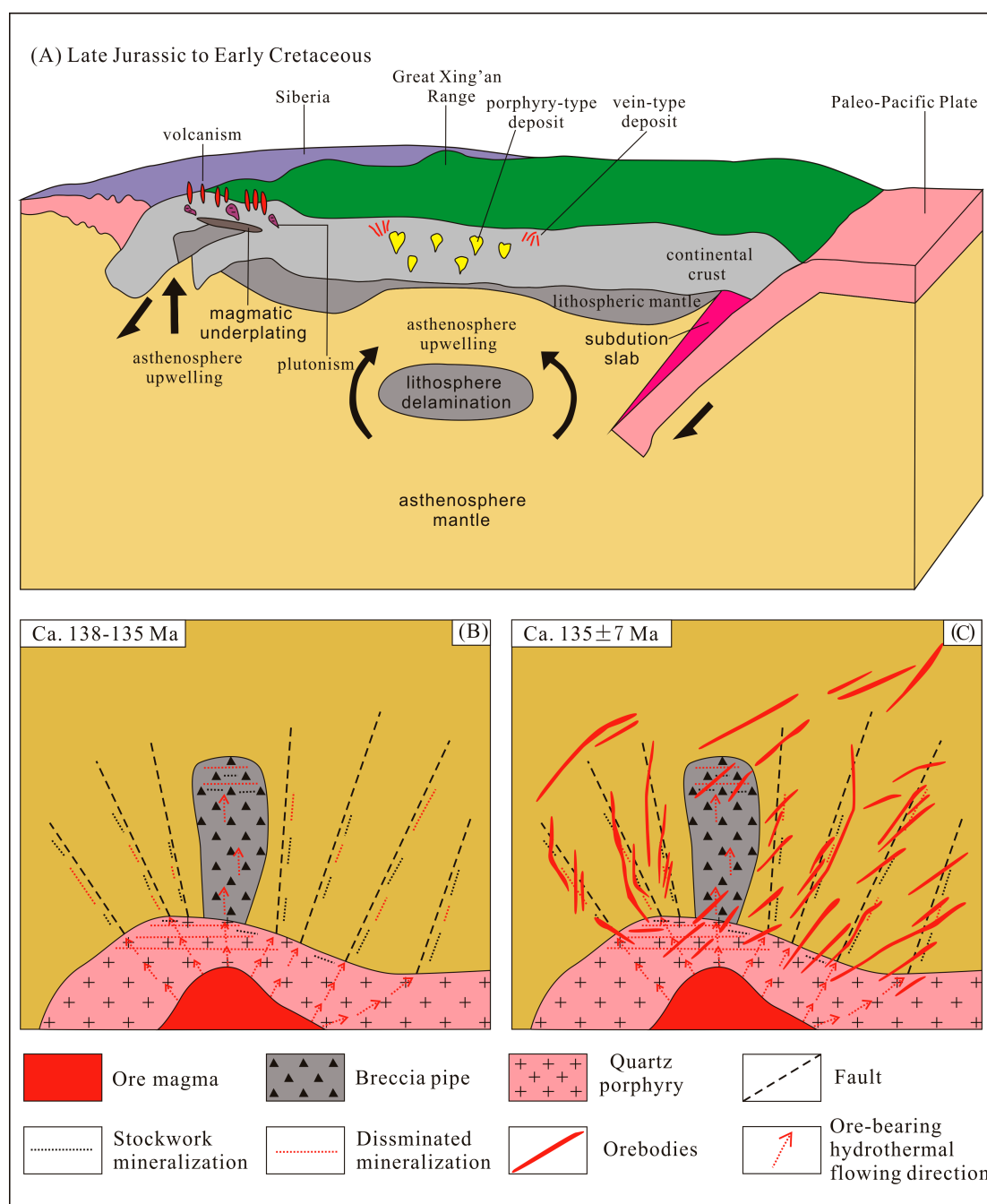


Figure 13. (A) Schematic model of the Late Jurassic to Early Cretaceous geodynamic evolution and associated ore deposits in the Great Xing'an Range. (B) Schematic model for the Weilasituo Sn-polymetallic deposit during 138–135 Ma. (C) Schematic model for the Weilasituo Sn-polymetallic deposit at 135 Ma.

7. Conclusions

Integrating zircon U-Pb and Re-Os dating, whole-rock geochemistry, and Hf isotopic data presented here with the results of previous research leads to the following conclusions:

- (1) The zircon U-Pb ages of the ore-forming porphyry (quartz porphyry) samples from the Weilasituo Sn-polymetallic deposit are 138.0 ± 1.1 Ma and 138.6 ± 1.1 Ma; the molybdenite Re-Os age is

135 ± 7 Ma. These ages date the metallogenesis of the deposit to the early stage of the Early Cretaceous at a time of transition from post-orogenic compression to extension following the subduction of the Paleo-Pacific Ocean.

- (2) The geochemistry data show that the ore-forming porphyry (quartz porphyry) of the deposit has high concentrations of SiO₂, Al₂O₃, and K₂O+Na₂O, and is a peraluminous, high-K calc-alkaline highly differentiated I-type granite by partial melting. Quartz porphyry has ε_{Hf}(t) values ranging from 1.90 to 6.90, corresponding to the T_{DM2} of 1069–747 Ma. The magmas were sourced from the juvenile lower crust mixed with mantle.
- (3) The ore-forming fluids of Sn-polymetallic mineralization were derived from partial melting of highly differentiated quartz porphyry. The interaction between ore-bearing hydrothermal fluids and surrounding rocks (“Xilin hot complex”) results in the precipitation of ore-forming elements.

Author Contributions: Conceptualization, F.Y. and J.S.; Investigation, F.Y., Y.W., J.F., F.N. and Z.F.; Data curation, F.Y.; Formal analysis, F.Y. and Z.H.; Funding acquisition, F.Y.; Project administration, J.S.; Writing—original draft preparation, F.Y.; Writing—review and editing, F.Y., J.S. and Y.W.

Funding: This research was funded by the National Natural Science Foundation of China (Grants No. 41172072) and the China Geological Survey (Grants No. DD20160048-01, DD20160048-16, DD20160048-05).

Acknowledgments: We thank the geologists from the Weilasituo Mining, Co. Ltd. with their assistance in the field work for the Weilasituo Sn-polymetallic deposit.

Conflicts of Interest: The authors declare no conflict of interest.

References

1. Zeng, Q.D.; Liu, J.M.; Qin, F.; Zhang, Z.L.; Chen, W.J. Preliminary research on Mesozoic four-stage Mo mineralization in Da Hinggan mountains of China. In Proceedings of the Gondwana 13th Program and Abstracts, Yunnan, China, 28 September 2008; pp. 251–252.
2. Meng, E.; Xu, W.L.; Yang, D.B.; Qiu, K.F.; Li, C.H.; Zhu, H.T. Zircon U-Pb chronology, geochemistry of Mesozoic volcanic rocks from the Lingquan basin in Maznhouli area, and its tectonics. *Acta Petrol. Sin.* **2011**, *27*, 1209–1226. (In Chinese)
3. Qin, K.Z.; Zhai, M.G.; Li, G.M.; Zhao, J.X.; Zeng, Q.D.; Gao, J.; Xiao, W.J.; Li, J.L.; Sun, S. Links of collage orogenesis of multiblocks and crust evolution to characteristic metallogenesis in China. *Acta Petrol. Sin.* **2017**, *33*, 305–325. (In Chinese)
4. Zhang, Z.D.; Wu, C.Z.; Gu, L.X.; Feng, H.; Zheng, Y.C.; Huang, J.H.; Li, J.; Sun, Y.L. Molybdenite Re-Os dating of Xintaimen molybdenum deposit in Yanshan-Liaoning metallogenic belt, North China. *Miner. Depos.* **2009**, *28*, 313–320. (In Chinese)
5. Chen, W.J.; Liu, J.M.; Liu, H.T.; Sun, X.G.; Zhang, R.B.; Zhang, Z.L.; Qin, F. Geochronology and fluid inclusion study of the Jiguanshan porphyry Mo deposit, Inner Mongolia. *Acta Petrol. Sin.* **2010**, *26*, 1423–1436. (In Chinese)
6. Deng, J.; Wang, C.M.; Bagas, L.; Carranza, E.J.M.; Lu, Y.J. Cretaceous-Cenozoic tectonic history of the Jiaojia Fault and gold mineralization in the Jiaodong Peninsula, China: Constraints from zircon U-Pb, illite K-Ar, and apatite fission track thermochronometry. *Miner. Depos.* **2015**, *50*, 987–1006. [[CrossRef](#)]
7. Zeng, Q.D.; Liu, J.M.; Chu, S.X.; Wang, Y.B.; Sun, Y.; Duan, X.X.; Zhou, L.L. Mesozoic molybdenum deposits in the East Xingmeng orogenic belt, northeast China: Characteristics and tectonic setting. *Inter. Geol. Rev.* **2012**, *54*, 1843–1869. [[CrossRef](#)]
8. Jiang, S.H.; Nie, F.J.; Bai, D.M.; Liu, Y.F.; Liu, Y. Geochronology evidence for Indosinian mineralization in Baiyinnuoer Pb-Zn deposit of Inner Mongolia. *Miner. Depos.* **2011**, *30*, 787–798. (In Chinese)
9. Zhu, X.Q.; Zhang, Q.; He, Y.L.; Zhu, C.H.; Huang, Y. Hydrothermal source rocks of the Meng’entaolegai Ag-Pb-Zn deposit in the granite batholith, Inner Mongolia, China. *Geochem. J.* **2006**, *40*, 265–275. [[CrossRef](#)]
10. Sheng, J.F.; Fu, X.Z. *The Geolocial Features of Copper-Polymetallic Deposit and the Ore-Forming Environment in Middle Part of the Greater Khingan Range*; Earthquake Press: Beijing, China, 1999; pp. 1–65. (In Chinese)
11. Zhang, K.; Nie, F.J.; Hou, W.R.; Li, C.; Liu, Y. Re-Os isotopic age dating of molybdenite separates from Hashitu Mo deposit in Linxi County of Inner Mongolia and its geological significance. *Miner. Depos.* **2012**, *31*, 129–138. (In Chinese)

12. Zhao, Y.M.; Zhang, D.Q. *Metallogeny and Prospective Evaluation of Copperpolymetallic Deposits in the Da Hinggan Mountains and Its Adjacent Regions*; Seismological Publishing House: Beijing, China, 1997; pp. 1–318. (In Chinese)
13. Zhao, Y.M.; Wang, D.W.; Zhang, D.Q.; Fu, X.Z.; Bao, X.P.; Ai, Y.F. *Ore-Controlling Factors and Ore-Prospecting Models for Copper-Polymetallic Deposits in Southeastern Inner Mongolia*; Seismological Publishing House: Beijing, China, 1994; pp. 1–234. (In Chinese)
14. Ishiyama, D.; Sato, R.; Toshio, M.; Yohei, I.; Wang, J.B. Characteristic features of tiniron- coppermineralization in the Anle-Huanggangliangmining area, InnerMongolia, China. *Resour. Geol.* **2008**, *51*, 377–392. [[CrossRef](#)]
15. Jiang, S.H.; Liang, Q.L.; Liu, Y.F.; Liu, Y. Zircon U-Pb ages of themagmatic rocks occurring in and around the Dajing Cu-Ag-Sn polymetallic deposit of Inner Mongolia and constrains to the ore-forming age. *Acta Petrol. Sin.* **2012**, *28*, 495–513. (In Chinese)
16. Liu, Y.F.; Jiang, S.H.; Bagas, L. The genesis of metal zonation in the Weilasituo and Bairendaba Ag-Zn-Pb-Cu-(Sn-W) deposits in the shallow part of a porphyry Sn-polymetal system, Inner Mongolia, China. *Ore Geol. Rev.* **2016**, *75*, 150–173. [[CrossRef](#)]
17. Wang, F.X.; Bagas, L.; Jiang, S.H.; Liu, Y.F. Geological, geochemical, and geochronological characteristics of Weilasituo Sn-polymetal deposit, Inner Mongolia, China. *Ore Geol. Rev.* **2017**, *80*, 1206–1229. [[CrossRef](#)]
18. Pan, X.F.; Guo, L.J.; Wang, S.; Xue, H.M.; Hou, Z.Q.; Tong, Y.; Li, Z.M. Laser microprobe Ar-Ar dating of biotite from the Weilasituo Cu-Zn polymetallic deposit in Inner Mongolia. *Acta Petrol. Miner.* **2009**, *28*, 473–479. (In Chinese)
19. Chang, Y.; Lai, Y. Study on characteristics of ore-forming fluid and chronology in the Yindu Zn-Pb-Ag polymetallic ore deposit, Inner Mongolia. *Acta Sci. Natl. Univ. Pekinensis* **2010**, *46*, 581–593. (In Chinese)
20. Zhou, Z.H. *Geology and Geochemistry of Huanggang Sn-Fe Deposit, Inner Mongolia*. Ph.D. Thesis, Chinese Academy of Geological Sciences, Beijing, China, 2011; pp. 1–182. (In Chinese)
21. Wang, C.Y. *Lead-Zinc Polymetallic Metallogenic Series and Prospecting Direction of Huanggangliang-Ganzhuermiao Metallogenic Belt, Inner Mongolia*. Ph.D. Thesis, Jilin University, Changchun, China, 2014; pp. 1–178. (In Chinese)
22. Wang, J.B.; Wang, Y.W.; Wang, L.J.; Uemoto, T. Tin-polymetallic mineralization in the southern part of the Da Hinggan Mountains, China. *Resour. Geol.* **2001**, *51*, 283–291. [[CrossRef](#)]
23. Zeng, Q.D.; Liu, J.M.; Zhang, Z.L. Re-Os geochronology of porphyry molybdenum deposit in south segment of Da Hinggan Mountains, Northeast China. *J. Earth Sci.* **2010**, *21*, 392–401. [[CrossRef](#)]
24. Nie, F.J.; Zhang, W.Y.; Du, A.D.; Jiang, S.H.; Liu, Y. Re-Os isotopic dating on molybdenite separates from the Xiaodonggou porphyry Mo deposit, Hexigten Qi, Inner Mongolia. *Acta Geol. Sin.* **2007**, *81*, 898–905. (In Chinese) [[CrossRef](#)]
25. Zhang, J.H.; Gao, S.; Ge, W.C.; Wu, F.Y.; Yang, J.H.; Wilde, S.A.; Li, M. Geochronology of the Mesozoic volcanic rocks in the Great Xing'an Range, northeastern China: Implications for subduction-induced delamination. *Chem. Geol.* **2010**, *276*, 144–165. [[CrossRef](#)]
26. Guo, F.; Fan, W.; Li, C.; Gao, X.; Miao, L. Early Cretaceous highly positive ϵ_{Nd} felsic volcanic rocks from the Hinggan Mountains, NE China: Origin and implications for Phanerozoic crustal growth. *Int. J. Earth Sci.* **2009**, *98*, 1395–1411. [[CrossRef](#)]
27. Zhai, D.G.; Liu, J.J.; Li, J.M.; Zhang, M.; Li, B.Y.; Fu, X.; Jiang, H.C.; Ma, L.J.; Qi, L. Geochronological study of Weilasituo porphyry type Sn deposit in Inner Mongolia and its geological significance. *Miner. Depos.* **2016**, *35*, 1011–1022. (In Chinese)
28. Liu, Y.F.; Fan, Z.Y.; Jiang, H.C.; Nie, F.J.; Jiang, S.H.; Ding, C.W.; Wang, F.Z. Genesis of the Weilasituo-Bairendaba Porphyry-Hydrothermal vein type system in Inner Mongolia, China. *Acta Geol. Sin.* **2014**, *88*, 2373–2385. (In Chinese)
29. Xu, W.L.; Wang, F.; Meng, E.; Gao, F.H.; Pei, F.P.; Yu, J.J.; Tang, J. Paleozoic-Early Mesozoic tectonic evolution in the Eastern Heilongjiang Province, NE China: Evidence from igneous rock association and U-Pb geochronology of detrital zircons. *J. Jilin Univ.* **2012**, *42*, 1378–1389. (In Chinese)
30. Sengör, A.M.C.; Natal'in, B.A.; Burtman, V.S. Evolution of the Altaid tectonic collage and Palaeozoic crustal growth in Eurasia. *Nature* **1993**, *364*, 299–307. [[CrossRef](#)]
31. Xiao, W.J.; Windley, B.F.; Hao, J.; Zhai, M.G. Accretion leading to collision and the Permian Solonker suture, Inner Mongolia, China: Termination of the central Asian orogenic belt. *Tectonics* **2003**, *22*, 1069. [[CrossRef](#)]

32. Xiao, W.J.; Li, S.Z.; Santosh, M.; Jahn, B.M. Orogenic belts in Central Asia: Correlations and connections. *J. Earth Sci.* **2012**, *49*, 1–6. [[CrossRef](#)]
33. Wu, F.Y.; Sun, D.Y.; Li, H.M.; Jahn, B.M.; Wilde, S.A. A-type granites in northeastern China: Age and geochemical constraints on their petrogenesis. *Chem. Geol.* **2002**, *187*, 143–173. [[CrossRef](#)]
34. Zhang, J.H.; Ge, W.C.; Wu, F.Y.; Wilde, S.A.; Yang, J.H.; Liu, X.M. Large-scale Early Cretaceous volcanic events in the northern Great Xing'an Range, northeastern China. *Lithos* **2008**, *102*, 138–157. [[CrossRef](#)]
35. Qin, G.J.; Kawachi, Y.; Zhao, L.Q.; Wang, Y.Z.; Ou, Q. The Upper Permian sedimentary facies and its role in the Dajing Cu-Sn deposit, Linxi County, Inner Mongolia, China. *Resour. Geol.* **2001**, *51*, 293–305. [[CrossRef](#)]
36. Shi, Y.R.; Liu, D.Y.; Zhang, Q.; Jian, P.; Zhang, F.Q.; Miao, L.C. SHRIMP geochronology of dioritic-granitic intrusions in Sunidzuoqi area, Inner Mongolia. *Acta Geol. Sin.* **2004**, *79*, 789–799. (In Chinese)
37. Zhang, X.H.; Wilde, S.A.; Zhang, H.F.; Zhai, M.G. Early Permian high-K calc-alkaline volcanic rocks from NW Inner Mongolia, North China: Geochemistry, origin and tectonic implications. *J. Geol. Soc.* **2011**, *168*, 525–543. [[CrossRef](#)]
38. Guo, F.; Fan, W.M.; Gao, X.F.; Li, C.W.; Miao, L.C.; Zhao, L.; Li, H.X. Sr-Nd-Pb isotope mapping of Mesozoic igneous rocks in NE China: Constraints on tectonic framework Phanerozoic crustal growth. *Lithos* **2010**, *120*, 563–578. [[CrossRef](#)]
39. Wang, Y.X.; Zhao, Z.H. Geochemistry and origin of the Baerzhe REE-Nb-Be-Zr super-large deposit. *Geochimica* **1997**, *26*, 24–35. (In Chinese)
40. Zhao, G.L.; Yang, G.L.; Fu, J.Y.; Wang, Z.; Fu, J.Y.; Yang, Y.Z. *Mesozoic Volcanic Rocks in Central and Southern Da Hinggan Ling Range*; Beijing Science and Technology Publishing House: Beijing, China, 1989; pp. 1–86. (In Chinese)
41. Deng, J.; Wang, Q.F.; Li, G.J.; Santosh, M. Cenozoic tectono-magmatic and metallogenic processes in the Sanjiang region, southwestern China. *Earth-Sci. Rev.* **2014**, 138268–138299. [[CrossRef](#)]
42. Zhong, R.C.; Yang, Y.F.; Shi, Y.X.; Li, W.B. Ore characters and ore genesis of the Bairendaba Ag polymetallic ore deposit in Keshiketeng banner, Inner Mongolia. *Geol. China* **2008**, *6*, 1–25. (In Chinese)
43. Yang, L.Q.; Deng, J.; Dilek, Y.; Qiu, K.F.; Ji, X.Z.; Li, N.; Taylor, R.D.; Yu, J.Y. Structure, Geochronology, and Petrogenesis of the Late Triassic Puziba Granitoid Dikes in the Mianlue Suture Zone, Qinling Orogen, China. *Geol. Soc. Am. Bull.* **2015**, *11–12*, 1831–1854. [[CrossRef](#)]
44. Du, A.D.; Wu, S.Q.; Sun, D.Z.; Wang, S.X.; Qu, W.J.; Markey, R.; Stain, H.; Morgan, J.; Malinovskiy, D. Preparation and certification of Re-Os dating reference materials: Molybdenites HLP and JDC. *Geostand. Geoanal. Res.* **2004**, *28*, 41–52. [[CrossRef](#)]
45. Wu, F.Y.; Yang, Y.H.; Xie, L.W.; Yang, J.H.; Xu, P. Hf isotopic compositions of the standard zircons and baddeleyites used in U-Pb geochronology. *Chem. Geol.* **2006**, *234*, 105–126. [[CrossRef](#)]
46. Yang, L.Q.; Deng, J.; Qiu, K.F.; Ji, X.Z.; Santosh, M.; Song, K.R.; Song, Y.H.; Geng, J.Z.; Zhang, C.; Hua, B. Magma mixing and crust-mantle interaction in the Triassic monzogranites of Bikou Terrane, central China: Constraints from petrology, geochemistry, and zircon U-Pb-Hf isotopic systematic. *J. Asian Earth Sci.* **2015**, *98*, 320–341. [[CrossRef](#)]
47. Woodhead, J.D.; Hergt, J.M. A preliminary appraisal of seven natural zircon reference materials for in situ Hf isotope determination. *Geostand. Geoanal. Res.* **2005**, *29*, 183–195. [[CrossRef](#)]
48. Scherer, E.; Munker, C.; Mezger, K. Calibration of the Lutetium-Hafnium clock. *Science* **2001**, *293*, 683–687. [[CrossRef](#)]
49. Blichert-Toft, J.; Albarède, F. The Lu-Hf geochemistry of chondrites and the evolution of the mantle-crust system. *Earth Planet. Sci. Lett.* **1997**, *148*, 243–258. [[CrossRef](#)]
50. Nowell, G.M.; Kempton, P.D.; Noble, S.R.; Fitton, J.G.; Saunders, A.D.; Mahoney, J.J.; Taylor, R.N. High precision Hf isotope measurements of MORB and OIB by thermal ionisation mass spectrometry: Insights into the depleted mantle. *Chem. Geol.* **1998**, *149*, 211–233. [[CrossRef](#)]
51. Griffin, W.L.; Pearson, N.J.; Belousova, E.; Jackson, S.E.; Van Achenbergh, E.; O'Reilly, S.Y.; Shee, S.R. The Hf isotope composition of cratonic mantle, LAM-MC-ICPMS analysis of zircon megacrysts in kimberlites. *Geochim. Cosmochim. Acta* **2000**, *64*, 133–147. [[CrossRef](#)]
52. Griffin, W.L.; Wang, X.; Jackson, S.E.; Pearson, N.J.; O'Reilly, S.Y.; Xu, X.S.; Zhou, X.M. Zircon chemistry and magma genesis, SE China: In-situ analysis of Hf isotopes, Tonglu and Pingtan igneous complexes. *Lithos* **2002**, *61*, 237–269. [[CrossRef](#)]

53. Peccerillo, A.; Taylor, S.R. Geochemistry of eocene calc-alkaline volcanic rocks from the Kastamonu area, Northern Turkey. *Contrib. Mineral. Petrol.* **1976**, *58*, 63–81. [[CrossRef](#)]
54. Maniar, P.D.; Piccoli, P.M. Tectonic discrimination of granitoids. *Geol. Soc. Am. Bull.* **1989**, *101*, 635–643. [[CrossRef](#)]
55. Middlemost, E.A.K. Naming materials in the magma/igneous rock system. *Earth Sci. Rev.* **1994**, *37*, 215–224. [[CrossRef](#)]
56. Middlemost, E.A.K. A simple classification of volcanic rocks. *Bull. Volcanol.* **1972**, *36*, 382–397. [[CrossRef](#)]
57. Boynton, W.V. Geochemistry of the rare earth elements, meteorite studies. In *Rare Earth Element Geochemistry*; Henderson, P., Ed.; Elsevier: Amsterdam, The Netherlands, 1984; pp. 63–114.
58. Sun, S.S.; McDonough, W.F. Chemical and isotopic systematics of oceanic basalts: Implications for mantle composition and processes. *Geol. Soc. Lond. Spec. Pub.* **1989**, *42*, 313–345. [[CrossRef](#)]
59. Lightfoot, P.C.; Hawkesworth, C.J.; Sethna, S.F. Petrogenesis of rhyolites and trachytes from the Deccan Trap: Sr, Nd and Pb isotope and trace element evidence. *Contrib. Mineral. Petrol.* **1987**, *95*, 44–54. [[CrossRef](#)]
60. Xiang, A.P.; Chen, Y.C.; Bagas, L. Molybdenite Re-Os and U-Pb zircon dating and genesis of the Dayana W-Mo deposit in eastern Ujumchin, Inner Mongolia. *Ore Geol. Rev.* **2016**, *78*, 268–280. [[CrossRef](#)]
61. Zhou, Z.H.; Mao, J.W. Geochronology and isotopic geochemistry of the A-type granites from the Huanggang Sn-Fe deposit, southern Great Hinggan Range, NE China: Implication for their origin and tectonic setting. *J. Asian Earth Sci.* **2012**, *49*, 272–286. [[CrossRef](#)]
62. Yang, Q.D.; Guo, L.; Wang, T.; Zeng, T.; Zhang, L.; Tong, Y.; Shi, X.J.; Zhang, J.J. Geochronology, origin, sources and tectonic settings of Late Mesozoic two-stage granites in the Ganzhuermiao region, central and southern Da Hinggan Range, NE China. *Acta Petrol. Sin.* **2014**, *30*, 1961–1981. [[CrossRef](#)]
63. Amelin, Y.; Lee, D.C.; Halliday, A.N. Early-middle Archean crustal evolution deduced from Lu-Hf and U-Pb isotopic studies of single zircon grains. *Geochim. Cosmochim. Acta* **2000**, *64*, 4205–4225. [[CrossRef](#)]
64. Vervoort, J.D.; Pachel, P.J.; Gehrels, G.E.; Nutman, A.P. Constraints on early Earth differentiation from hafnium and neodymium isotopes. *Nature* **1996**, *379*, 624–627. [[CrossRef](#)]
65. Yang, L.Q.; Deng, J.; Goldfarb, R.J.; Zhang, J.; Gao, B.F.; Wang, Z.L. ⁴⁰Ar/³⁹Ar geochronological constraints on the formation of the Dayingezhuang gold deposit: New implications for timing and duration of hydrothermal activity in the Jiaodong gold province, China. *Gondwana Res.* **2014**, *25*, 1469–1483. [[CrossRef](#)]
66. Yang, L.Q.; Deng, J.; Wang, Z.L.; Guo, L.N.; Li, R.H.; Groves, D.I.; Danyushevsky, L.V.; Zhang, C.; Zheng, X.L.; Zhao, H. Relationships between gold and pyrite at the Xincheng gold deposit, Jiaodong Peninsula, China: Implications for gold source and deposition in a brittle epizonal environment. *Econ. Geol.* **2016**, *111*, 105–126. [[CrossRef](#)]
67. Qiu, K.F.; Deng, J. Petrogenesis of granitoids in the Dewulu skarn copper deposit: Implication for the evolution of the Paleotethys ocean and mineralization in Western Qinling, China. *Ore Geol. Rev.* **2017**, *90*, 1078–1098. [[CrossRef](#)]
68. Sun, J.G.; Zhang, Y.; Han, S.J.; Men, L.J.; Li, Y.X.; Chai, P.; Yang, F. Timing of formation and geological setting of low-sulphidation epithermal gold deposits in the continental margin of NE China. *Int. Geol. Rev.* **2013**, *55*, 142–161. [[CrossRef](#)]
69. Qiu, K.F.; Deng, J.; Taylor, R.D.; Song, K.R.; Song, Y.H.; Li, Q.Z.; Goldfarb, R.J. Paleozoic magmatism and porphyry Cu-mineralization in an evolving tectonic setting in the North Qilian Orogenic Belt, NW China. *J. Asian Earth Sci.* **2016**, *122*, 20–40. [[CrossRef](#)]
70. Wu, F.Y.; Lin, J.Q.; Wilde, S.A.; Sun, D.Y.; Yang, J.H. Nature and significance of the Early Cretaceous giant igneous event in eastern China. *Earth Planet. Sci. Lett.* **2005**, *233*, 103–119. [[CrossRef](#)]
71. Mao, J.W.; Wang, Z.L. A preliminary study on time limits and geodynamic setting of largescale metallogeny in East China. *Miner. Depos.* **1999**, *19*, 289–296. (In Chinese)
72. Mao, J.W.; Konopelko, D.; Seltmann, R.; Lehmann, B.; Chen, W.; Wang, Y.T.; Eklund, O.; Usabaliev, T. Post collisional age of the Kumtor gold deposit and timing of Hercynian events in the Tien Shan, Kyrgyzstan. *Econ. Geol.* **2004**, *99*, 1771–1780. [[CrossRef](#)]
73. Qiu, K.F.; Marsh, E.; Yu, H.C.; Pfaff, K.; Gulbransen, C.; Gou, Z.Y.; Li, N. Fluid and metal sources for the Wenquan porphyry molybdenite deposit, Western Qinling, NW China. *Ore Geol. Rev.* **2017**, *86*, 459–473. [[CrossRef](#)]
74. Schiano, P.; Monzier, M.; Eissen, J.P.; Martin, H.; Koga, K.T. Simple mixing as the major control of the evolution of volcanic suites in the Ecuadorian Andes. *Contrib. Mineral. Petrol.* **2010**, *160*, 297–312. [[CrossRef](#)]

75. Pearce, J.A.; Harris, N.B.W.; Tindle, A.G. Trace element discrimination diagrams for the tectonic interpretation of granitic rocks. *J. Petrol.* **1984**, *25*, 956–983. [[CrossRef](#)]
76. Sylvester, P.J. Post-collisional strongly peraluminous granite. *Lithos* **1998**, *45*, 29–44. [[CrossRef](#)]
77. Chappell, B.W.; White, A.J.R. I-type and S-type granites in the Lachlan Fold Belt. *Trans. R. Soc. Ed. Earth Sci.* **1992**, *83*, 1–26. [[CrossRef](#)]
78. Ballouard, C.; Poujol, M.; Boulvais, P.; Branquet, Y.; Tartese, R.; Vigneresse, J.L. Nb-Ta fractionation in peraluminous granites: A marker of the magmatic-hydrothermal transition. *Geology* **2016**, *44*, 231–234. [[CrossRef](#)]
79. Breiter, K.; Lamas, C.N.; Borges, R.M.K.; Dall’Agnol, R. Chemical characteristics of zircon from A-type granites and comparison to zircon of S-type granites. *Lithos* **2014**, *192–195*, 208–225. [[CrossRef](#)]
80. Chen, J.Y.; Yang, J.H. Petrogenesis of the Fogang highly fractionated I-type granitoids: Constraints from Nb, Ta, Zr and Hf. *Acta Geol. Sin.* **2015**, *31*, 846–854. (In Chinese)
81. Whalen, J.B.; Currie, K.L.; Chappell, B.W. A-type granites: Geochemical characteristics, discrimination and petrogenesis. *Contrib. Mineral. Petrol.* **1987**, *95*, 407–419. [[CrossRef](#)]
82. Eby, G.N.; Woolley, A.R.; Din, V.; Platt, G. Geochemistry and petrogenesis of nepheline syenite. Kasungu-Chipala, Ilomba, and Ulindi nepheline syenite intrusions, North Nyasa Alkaline Province, Malawi. *J. Petrol.* **1990**, *39*, 1405–1424. [[CrossRef](#)]
83. Watson, E.B.; Harrison, T.M. Zircon saturation revisited: Temperature and composition effects in a variety of crustal magma types. *Earth Planet. Sci. Lett.* **1983**, *64*, 295–304. [[CrossRef](#)]
84. Zhu, J.C.; Rao, B.; Xiong, X.L.; Li, F.C.; Zhang, P.H. Comparison and genetic interpretation of Li-F rich, rare-metal bearing granitic rocks. *Geochimica* **2002**, *31*, 141–152. (In Chinese)
85. Liu, W.; Pan, X.F.; Xie, L.W.; Li, H. Sources of material for the Linxi granitoids, the southern segment of the Da Hinggan Mts.: When and how continental crust grew? *Acta Petrol. Sin.* **2007**, *23*, 441–460. (In Chinese)
86. Poli, G.E.; Tommasini, S. Model for the origin and significance of microgranular enclaves in calc-alkaline granitoids. *J. Petrol.* **1991**, *32*, 657–666. [[CrossRef](#)]
87. Qiu, K.F.; Yu, H.C.; Gou, Z.Y.; Liang, Z.L.; Zhang, J.L.; Zhu, R. Nature and origin of Triassic igneous activity in the Western Qingling Orogen: The Wenquan composite pluton example. *Int. Geol. Rev.* **2018**, *60*, 242–266. [[CrossRef](#)]
88. König, S.; Münker, C.; Hohl, S.; Paulick, H.; Barth, A.R.; Lagos, M.; Pfänder, J.; Büchl, A. The Earth’s tungsten budget during mantle melting and crust formation. *Geochim. Cosmochim. Acta* **2011**, *75*, 2119–2136. [[CrossRef](#)]
89. Qiu, K.F.; Taylor, R.D.; Song, Y.H.; Yu, H.C.; Song, K.R.; Li, N. Geologic and geochemical insights into the formation of the Taiyangshan porphyry copper-molybdenum deposit, Western Qinling Orogenic Belt, China. *Gondwana Res.* **2016**, *35*, 40–58. [[CrossRef](#)]
90. Chen, Y.J.; Pirajno, F.; Qi, J.P. Origin of gold metallogeny and sources of oreforming fluids, Jiaodong province, eastern China. *Int. Geol. Rev.* **2005**, *47*, 530–549. [[CrossRef](#)]
91. Chen, Y.J.; Fu, S.G. *Mineralization of Gold Deposits in West Henan*; China Seismological Press: Beijing, China, 1992; pp. 1–234. (In Chinese)
92. Kuzmin, M.L.; Abramovich, G.Y.A.; Dril, S.L.; Kravchisky, V.Y.A. The Mongolian–Okhotsk suture as the evidence of late Paleozoic–Mesozoic collisional processes in Central Asia. In Proceedings of the Abstract of 30th International Geological Congress, Beijing, China, 4–14 August 1996; Volume 1, p. 261.
93. Deng, J.; Wang, Q.F. Gold mineralization in China: Metallogenic provinces, deposit types and tectonic framework. *Gondwana Res.* **2016**, *36*, 219–274. [[CrossRef](#)]
94. Eugster, H.P. Granites and hydrothermal ore deposits: A geochemical framework. *Mineral. Mag.* **1985**, *49*, 7–23. [[CrossRef](#)]
95. Dingwell, D.B. The structure and properties of fluorine-rich magmas: A review of experimental studies. *Can. Inst. Min. Metall.* **1985**, *39*, 1–12.

